Volume 54
Number 9
7 May 2025
Pages 4089–4618

Chem Soc Rev

Chemical Society Reviews

rsc.li/chem-soc-rev

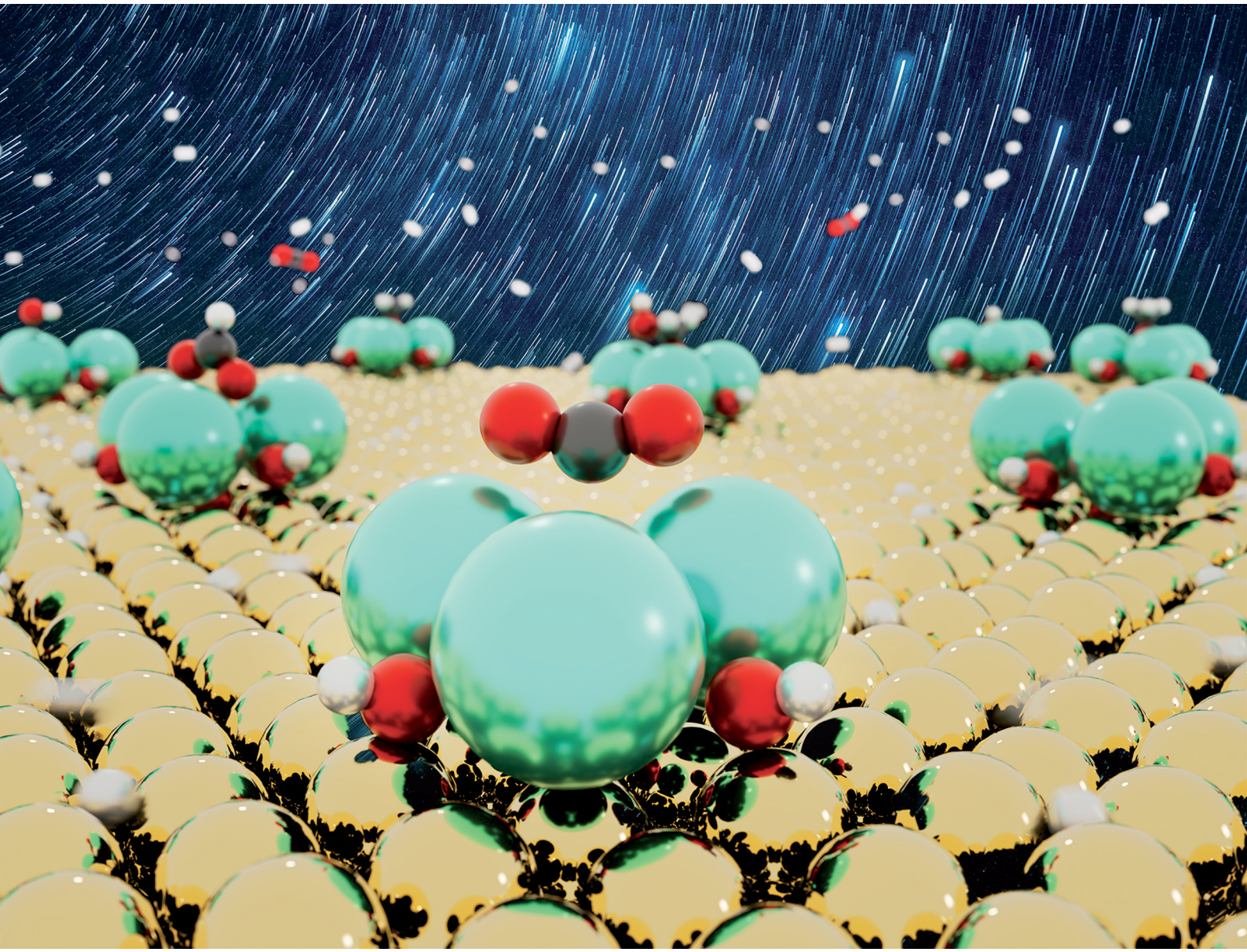

ISSN 0306-0012

ROYAL SOCIETY OF CHEMISTRY

REVIEW ARTICLE

Wenjie Liao, Ping Liu *et al.*

Alkali-induced catalytic tuning at metal and metal oxide interfaces

Chem Soc Rev

REVIEW ARTICLE

View Article Online
View Journal | View Issue

Cite this: *Chem. Soc. Rev.*, 2025, **54**, 4164

Alkali-induced catalytic tuning at metal and metal oxide interfaces

Wenjie Liao, *[a] An Nguyen[b] and Ping Liu *[ab]

Alkali metals have been recognized as effective promoters in heterogeneous catalysis, capable of enhancing catalytic activity and tuning product distributions. Over the past few decades, significant efforts have been made aiming to reveal the mechanisms underlying the promoting effect of alkalis. However, the roles that alkali metals play in the catalytic process remain elusive due to challenges in capturing their catalytic behaviours upon exposure to reactive environments. This review summarizes recent surface science and theoretical studies of alkali (potassium, cesium)-decorated metal and metal oxide model catalysts, revealing the crucial tuning by alkalis of activity and selectivity for CO_2 hydrogenation. The analysis of electronic structures identifies the selective binding mechanism of the positively charged alkali ions on the surface, being able to reduce the surface work function and lead to strong electron polarization on the surfaces. Depending on the alkali–support interaction, the deposition of alkalis can selectively modify the bindings of reaction intermediates involved in CO_2 hydrogenation *via* the interplay among the ionic, covalent and electrostatic tunings. As a result, CO_2 can be effectively activated and converted into diverse products at the alkali–support interface, ranging from formic acid to methanol and ethanol. The identified selective bond-tuning advances the application of alkalis in promoting catalytic activity and controlling catalytic selectivity at alkali–support interfaces.

Received 31st October 2024

DOI: 10.1039/d4cs01094a

rsc.li/chem-soc-rev

1. Introduction

Alkali metals, especially potassium (K) and cesium (Cs), have been widely used as promoters to tune the activity and selectivity of heterogenous catalysts for many crucial chemical processes such as Fischer–Tropsch synthesis (FTS), water–gas shift reactions, methanol (CH_3OH) synthesis from carbon monoxide (CO)/carbon dioxide (CO_2) hydrogenation, and ammonia synthesis.[1–9] It has been reported previously through both experimental[10–14] and theoretical studies[15–25] that doping with alkali metals enables tuning of the adsorption and dissociation of molecules, such as CO,[10,26] CO_2,[11,27] oxygen (O_2),[16,28,29]

[a] *Chemistry Division, Brookhaven National Laboratory, Upton, NY 11973, USA. E-mail: wliao@bnl.gov, pingliu3@bnl.gov*
[b] *Department of Chemistry, Stony Brook University, Stony Brook, NY 11794, USA*

Wenjie Liao

Wenjie Liao received his BS in Chemical Engineering from Tianjin University in 2017 and earned his PhD in Chemistry from Stony Brook University in 2023 under the supervision of Dr Ping Liu. He is currently a postdoctoral researcher in Dr Ping Liu's group at Brookhaven National Laboratory. His research focuses on employing computational chemistry tools and machine learning models to understand the nature of active sites, identify the operational reaction pathways, and promote catalytic performance in the conversion of C1 molecules.

An Nguyen

Phuc-An Nguyen earned a BS in Integrated Science from Fulbright University Vietnam in Saigon in 2023 as part of the institution's inaugural graduating class. Currently, Nguyen is a second-year PhD candidate in Chemistry at Stony Brook University, working under the guidance of Dr Ping Liu. As a researcher in Dr Liu's group at Brookhaven National Laboratory, Nguyen leverages computational chemistry techniques and machine learning methodologies to explore the nature of catalytic active sites, elucidate key reaction mechanisms, and enhance catalytic efficiency.

nitrogen (N_2),[7,30] and water (H_2O),[22,31,32] at the transition metal sites. So far, there has been no generally accepted mechanism to pinpoint the origin of the catalytic promoting effects of alkalis. Alternatively, several mechanisms have been proposed for the alkali-induced bond-tuning, including (1) electronic effects that modify the electronic structure of neighbouring transition metal sites *via* electron transfer from the alkali;[12,33–35] (2) reduction of the work function on transition metal surfaces,[36–39] thus affecting the ionization potential and Lewis basicity;[40,41] (3) electrostatic effects *via* dipole–dipole interactions between positively charged alkali ions and polarized adsorbates;[10,15–17,42] (4) steric effects including active site blocking[20,43,44] that inhibit adsorption of intermediates,[17] and surface reconstruction;[45] (5) synergistic or ensemble effects between alkalis and neighboring active sites which are necessary to provide effective binding to the reaction intermediates.[33]

The understanding of how alkalis function during catalytic processes is hindered by limited understanding of configurations of alkali deposits and their binding conformations with reaction intermediates under reaction conditions. This is extremely difficult to achieve at an atomic level using the current experimental tools. Instead, diverse structures have been proposed theoretically, which may not be directly relevant to the catalysis. Alkali promoters typically present in the form of oxides or salts with various morphologies rather than metallic phases upon interaction with reactive environments, which is often accompanied by structural changes. Accurate description of such complex transitions is crucial to elucidate the alkali-induced variation in reaction mechanisms and catalytic performances, which can greatly promote rational catalyst design using alkalis.

The present review discusses the recent surface science and theoretical studies of alkali-induced tuning effects in heterogenous catalysis, providing a bottom-up understanding going from surface morphology, electronic and atomic structures, and binding properties to catalytic activity and selectivity. CO_2 hydrogenation on metal and metal oxide catalysts was focused, which is of catalytic interest due to the importance in converting greenhouse gases into value-added chemicals. In particular, the production of methanol ($CO_2 + 3H_2 \rightarrow CH_3OH + H_2O$, $\Delta H = -49.5$ kJ mol^{-1}) has attracted considerable attention. The current industrial catalyst for CH_3OH synthesis from CO_2 hydrogenation, Cu–Zn/Al_2O_3, suffers from a low CO_2 conversion rate and CH_3OH selectivity due to the side reaction, reverse water–gas-shift reaction (RWGS: $CO_2 + H_2 \rightarrow CO + H_2O$, $\Delta H = 41.2$ kJ mol^{-1}).[46–48] According to previous studies on metallic Cu surfaces and nanoparticles,[49–51] the CH_3OH yield could be improved by stabilizing the key intermediates, *e.g.* *CO_2, formic acid (*HCOOH), carbon monoxide (*CO), or formyl (*CHO). Extensive studies have focused on optimizing the binding energy of these key intermediates and thus the activity of Cu using metal dopants[50,51] or oxide promoters,[48,52–56] while the promoting effect on alcohol selectivity is rather small and CO remains the major product. Cs has been reported to be an efficient promoter for CO_2 hydrogenation particularly on Cu-based catalysts,[57] not only promoting the adsorption and activation of CO_2,[26,58–60] but also enhancing the selectivity of CH_3OH,[61–63] ethanol (C_2H_5OH) and other higher alcohols.[64–66] In addition, well distributed K over Cu/SiO_2 was also found to facilitate CO_2 conversion,[67] while the CH_3OH selectivity was enhanced by the addition of K during CO hydrogenation over unsupported Cu catalysts.[68,69] Yet, the roles that Cs and K play during the CO_2 hydrogenation is less understood.

This review rationalizes how the multiple active sites at the alkali–support interfaces behave to tune the reaction mechanism, and explores the general design principle, challenges and opportunities in optimizing alkali–support interfaces towards selective CO_2 conversion to alcohols. CO_2 hydrogenation is rather complex, and typically involves multiple pathways, including formate, RWGS, CO hydrogenation and methanation pathways, as well as products, including methane (CH_4), CO, HCOOH, formaldehyde (CH_2O) and alcohols (*i.e.*, CH_3OH and C_2H_5OH, Fig. 1). Product separation can be cost effective in practical applications. Thus, the selectivity was focused on here, that is, tuning the alkali–support interface to improve CO_2 hydrogenation toward CH_3OH and higher alcohols, which are chemically more valuable than CO and CH_4. This review first summarizes the morphologies of alkali-decorated surfaces upon exposure to reactive environments. This summary is followed by identification of the tunable binding nature of alkali sites *via* alkali–support interactions and the corresponding impact on catalytic selectivity during CO_2 hydrogenation. Finally, the challenges and opportunities for optimizing alkali–support interfaces to advance selective CO_2 hydrogenation are discussed.

Ping Liu

Ping Liu is a senior chemist in the Chemistry Division, Brookhaven National Laboratory and an adjunct faculty member of the Chemistry Department, Stony Brook University. Her research focuses on theoretical description of multifunctional catalysts and their catalytic applications in heterogeneous catalysis and electrocatalysis, going from a fundamental understanding of catalytic processes under reaction conditions to providing guidance for catalyst design. Dr Liu has been recognized as a Highly Cited Researcher in Cross-Field research by Clarivate Analytics.

2. Morphology of alkali-decorated metal surfaces

2.1. K on Cu(111)

Decoration with K has played essential roles in promoting catalytic reactions in many established industrial catalytic

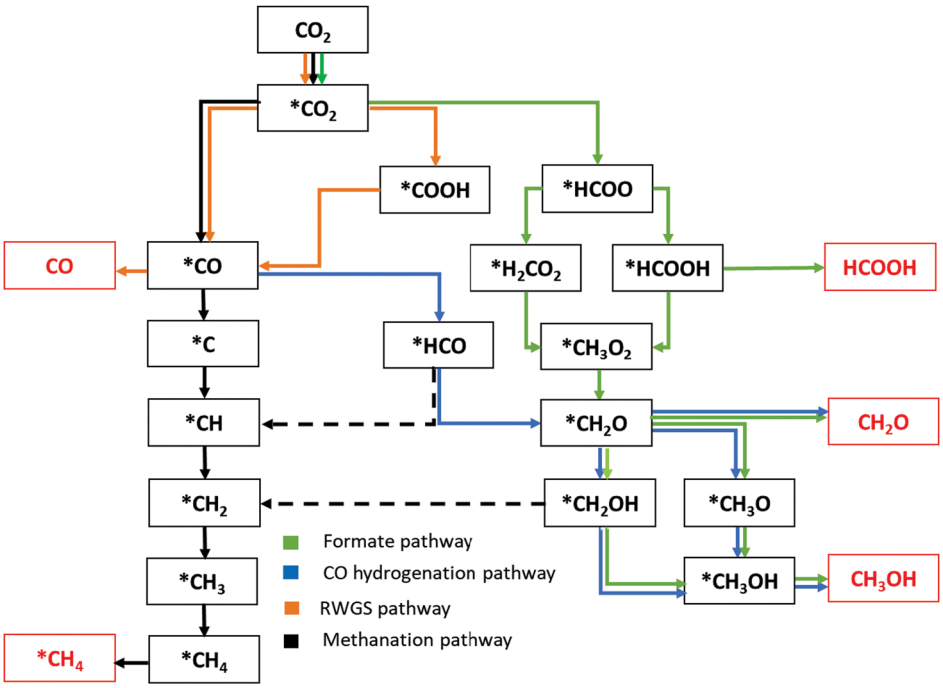

Fig. 1 Schematics of the reaction network for CO_2 hydrogenation to C_1 products. "*X" represents an adsorbed species on the surface.

processes including WGS, Haber–Bosch and FTS processes.[70–72] A combined density functional theory (DFT) and scanning tunneling microscopy (STM) study showed that both K and Cu(111) undergo oxidation, and deposition of K leads to the further oxidation of Cu_xO film supported on Cu(111) or K/Cu_xO/Cu(111) ($x \leq 2$) by sequential annealing under an oxygen atmosphere (Fig. 2a).[73] The DFT calculations identified a pseudomorphic growth mode, which is mainly controlled by strong interaction with chemisorbed oxygen at the center of the $O^{\delta-}$–$Cu^{\delta+}$–$O^{\delta-}$ hexagonal ring. The coverage can reach up to 0.19 monolayer (ML), which is consistent with the STM observations (Fig. 2b).

The deposition of K has a significant impact on the surface electronic structure of Cu_xO/Cu(111).[73] A reduction in work function from 5.3 eV to 2.0 eV was observed. This leads to strong electron polarization on the surfaces in a selective way, that is, enhancing the Lewis basicity of the surface, but hardly altering the weak Lewis acidity (Fig. 2c). As a result, the tuning of K on the chemical activities of Cu_xO/Cu(111) is selective. For bindings of CO and CO_2 involved in CO oxidation, the K-induced effect destabilizes *CO (ΔBE = 0.25 eV), but stabilizes $*CO_2$ binding in a bent O═C═O motif (ΔBE = −0.22 eV, Table 1) compared with Cu_xO/Cu(111). In both cases, the deposited K donates electrons to Cu_xO/Cu(111) (electronic effect) and there is a synergy between K sites and Cu sites to accommodate the O anchor *via* electrostatic $O^{\delta-}$–$K^{\delta+}$ interaction and C anchor *via* Cu–C interaction (ensemble effect, Fig. 2d and e). While the opposite bond-tuning is likely dominated by the K-induced reduction in work function and accumulation of electron densities over the surface of Cu_xO/Cu(111), which facilitates charge transfer to $*CO_2$ and formation of stable carboxylic-like species, but destabilizes *CO likely due to the nature of weak electron-acceptor and weak C–$Cu^{\delta+}$ interactions (Fig. 2d).

2.2. K on Au(111)

The situation for K deposition on Au(111) is different from that of Cu(111). Upon deposition of K under an oxygen atmosphere on Au(111), small KO_x clusters at low K loading were observed at the undercoordinated elbow sites of the herringbone reconstruction by scanning tunneling microscopy (STM) (Fig. 3a).[75] At low temperature (<305 Kelvin), the formation of K_2O_2 on Au(111) is preferred by dissociative O_2 adsorption at a K coverage of 0.125 ML ($2*K + O_2(g) \rightarrow *K_2O_2 + *$, Fig. 3b) according to the phase diagram that was calculated using DFT. Herein, the O–O bond distance in $*K_2O_2$ (1.46 Å) is closer to a peroxo (1.49 Å) instead of a superoxo (1.28 Å) which well describes the STM data collected at ∼0.1 ML coverage.[15]

As temperature increases (300–465 Kelvin), the O–O bond dissociation of K_2O_2 and subsequent reduction by metallic K becomes favorable ($1/2*K_2O_2 + *K \rightarrow *K_2O$, Fig. 3b), leading to the formation of K_2O/Au(111) (Fig. 3a, left column). At higher temperatures (>465 Kelvin), the entropic contribution of O_2 dominates the thermodynamics, which drives the decomposition of $*K_2O_2$ to $*K_2O$ ($K_2O_2 \rightarrow *K_2O + 1/2O_2(g)$, Fig. 3b). Meanwhile, the formation of K_2O_2 is no longer a thermodynamic spontaneous process, so K_2O_2 is not a stable phase at this elevated temperature. At medium to high K coverage (∼0.2 ML, Fig. 3a), small KO_x clusters can aggregate to form large islands as observed in STM, which likely adopts K_3O_3 overlayer on Au(111) according to the DFT calculations.[75] Notably, the K^+ ions are arranged in a hexagonal overlayer corresponding to a periodicity of 8.8 Å. Such hexagonal

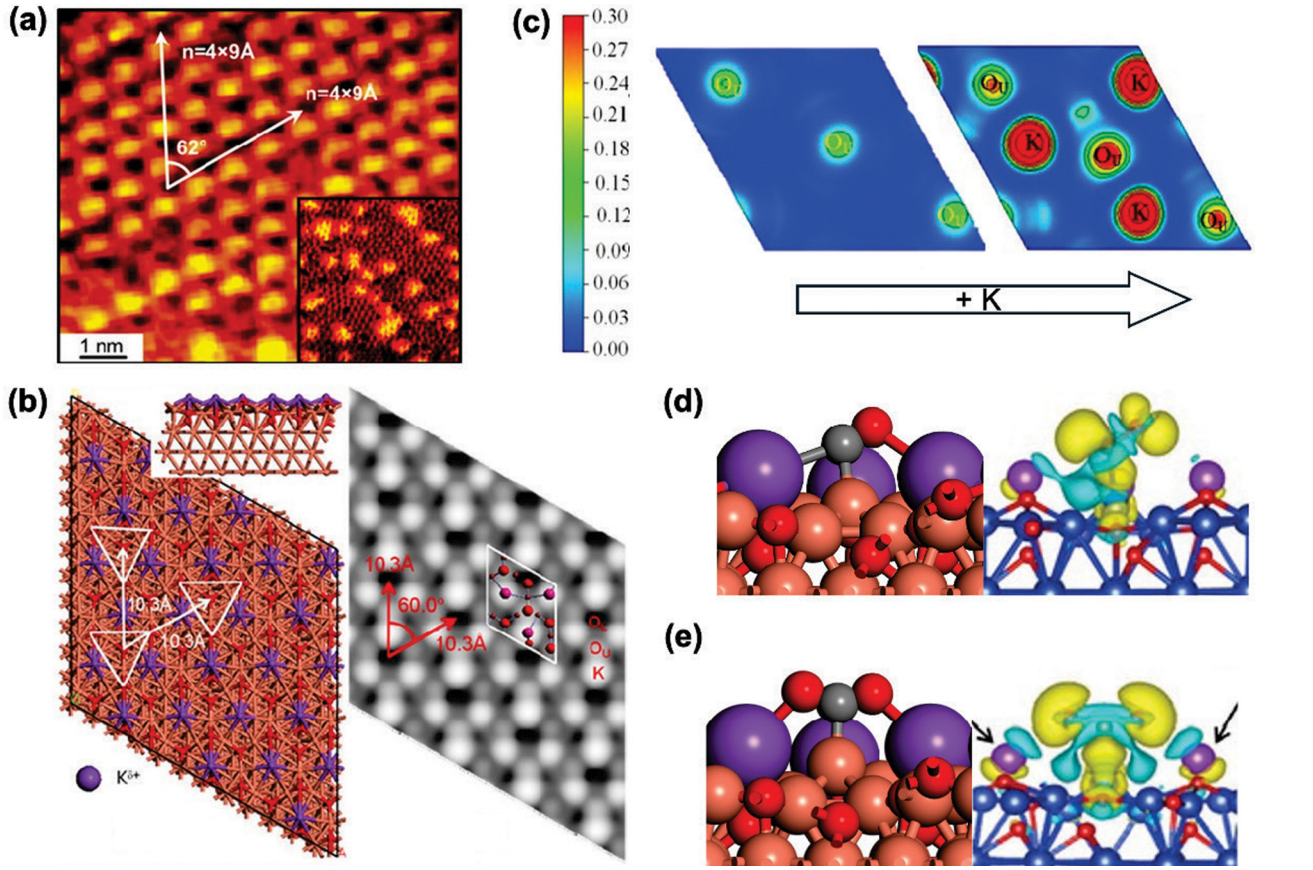

Fig. 2 (a) STM image of the K/Cu_xO/Cu(111) surface scanned at room temperature, which is followed by sequential annealing in 5×10^{-7} Torr O_2 at 500 K for 10 min: 0.87 nA, 1.68 V. Inset: A 20 × 20 nm^2 STM image of the surface prepared by room temperature deposition: 0.52 nA, 0.49 V. (b) DFT-optimized structure for K/Cu_xO/Cu(111) and the corresponding simulated STM image in constant current mode at −1.2 V sample bias. (c) Calculated electron localization function (ELF) of the Cu_xO/Cu(111) before (left) and after (right) the deposition of K, in which the projected 2D slices over and normal to the surface are displayed. The iso-surface level was chosen as $0.3e/a_0^3$ (a_0 represents Bohr radius). Side views of DFT optimized structures for (d) *CO and (e) *CO_2 on K/Cu_xO/Cu(111) with the calculated charge density difference. Color code: red – O; brown – Cu; purple – K; grey – C; yellow iso-surfaces – charge accumulation; cyan iso-surfaces – charge depletion at $0.001e/a_0^3$ (a_0: Bohr radius). Copyright 2015, Wiley.[73]

Table 1 DFT calculated binding energy (BE) comparison for the selected species on Cu(111), $Cs_3O_4H_3$/Cu(111), K/Cu_xO/Cu(111), K_2O/Au(111), and $Cs_3O_4H_3$/Au(111) surfaces

	BE (eV)				
Species	Cu(111)[74]	$Cs_3O_4H_3$/Cu(111)[66]	K/Cu_xO/Cu(111)[74]	K_2O/Au(111)[75]	$Cs_3O_4H_3$/Au(111)[76]
*CO_2	−0.06	−0.86	−0.32	−0.40	−0.03
*HCOO	−2.84	−3.50	−3.75	—	−2.98
*COOH	−1.66	−1.53	−2.39	—	−0.84
*H_2COO	−4.03	−3.55	−3.66	—	−2.40
*HCOOH	−0.24	−0.41	−0.84	—	−0.36
*H_2COOH	−2.19	−2.84	−2.66	—	−2.17
*$H_2C(OH)_2$	−0.25	−0.50	−0.92	—	−0.42
*CO	−0.89	−0.17	−0.41	−0.13	−0.04
*CHO	−1.29	−0.73	—	—	−0.21
*CH_2O	−0.11	−0.27	−0.51	—	−0.15
*CH_3O	−2.44	−2.33	−2.42	—	−1.81
*CH_3OH	−0.29	−0.40	−0.85	—	−0.34
*OH	−2.92	−3.55	−3.41	−2.57	−2.60
*H_2O	−0.24	−0.48	−0.94	−0.88	−0.49

conformation cannot be maintained in other K_3O_y/Au(111) (y = 1, 2, 4, 5, 6) overlayer systems, which often require the rearrangement of K and interacted Au to maximize their oxygen coordination.

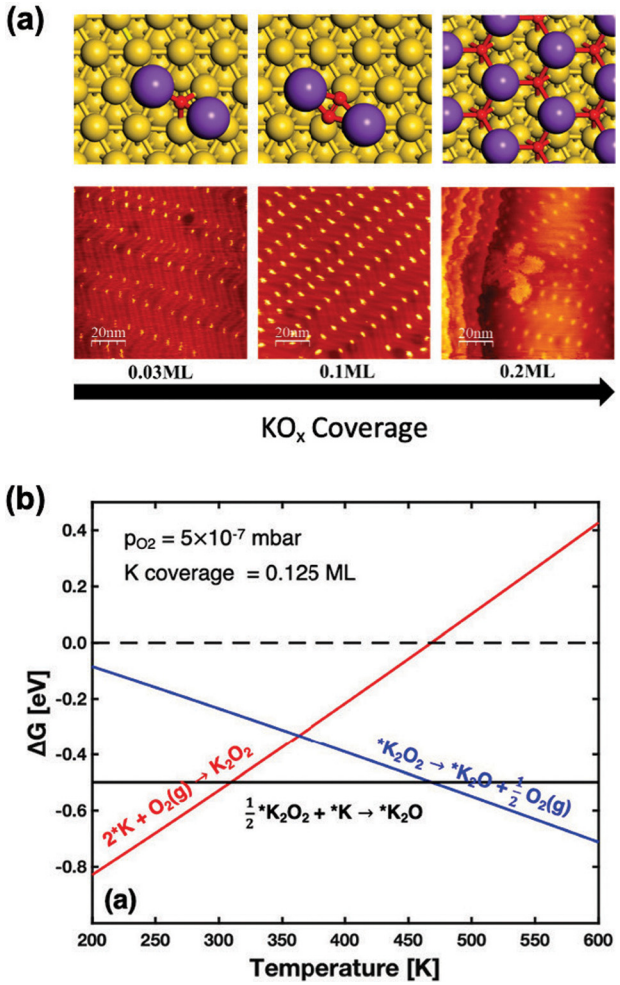

Fig. 3 (a) The multiple growth modes of potassium oxide modelled by DFT calculations (upper row) and observed by STM (lower row). Color code: purple – K; gold – Au; red – O. (b) Calculated phase diagram of potassium oxide species on Au(111) under oxidation conditions. Copyright 2022, Wiley.[75]

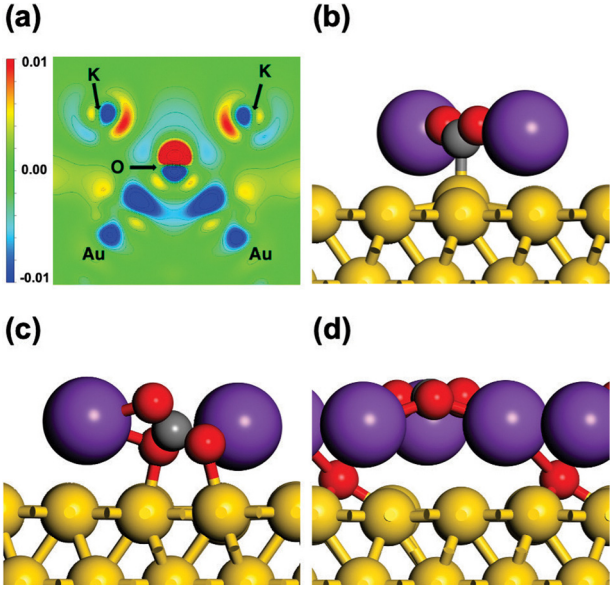

Fig. 4 (a) Contour plot of charge density difference for K_2O/Au(111). The blue region and red region indicate the accumulation and depletion of electron density, respectively. Side views of the DFT optimized structures for (b) *CO_2 on K_2O/Au(111), (c) *CO_3 on K_2O/Au(111), and (d) *CO_3 on K_3O_3/Au(111). Color code: purple – K; gold – Au; red – O; grey – C. Copyright 2022, Wiley.[77]

Using CO oxidation as a probing reaction, it was observed experimentally that the rate of CO_2 production on exposure to 4 Torr of CO and 2 Torr of O_2 at 473 Kelvin is zero on Au(111) and reaches a maximum around 0.1 ML of KO_x on Au(111).[75] When the coverage of KO_x goes above 0.15 ML, the activity starts to drop. Under this condition, K_2O/Au(111) is likely formed according to the DFT-calculated phase diagram (Fig. 3b), which displays an optimal activity and resistance to deactivation by carbonate (*CO_3), a potential poison, as compared to K_2O_2/Au(111) and K_3O_3 overlayer/Au(111).

Due to accumulated electron density on the top of $O^{\delta-}$ (Fig. 4a), the oxygen site acts as a strong anchor for CO to facilitate the production of *CO_2 (BE = −0.40 eV, Fig. 4b and Table 1) *via* the Mars–van-Krevelen (MvK) mechanism. In addition, due to the limited oxygen available for *K_2O, the formation of *CO_3 is hindered (BE = −0.85 eV, Fig. 4b). While with the decreased K : O ratio, *K_2O_2 and *K_3O_3 can provide more oxygen, tuning the selectivity gradually from CO_2 toward *CO_3 (BE = −2.34 eV, Fig. 4c and d). This is well demonstrated by the experimentally observed decrease in activity at high K coverage. Herein, both Au and KO_x participate in binding, as seen for K/Cu_xO/Cu(111) (Fig. 2). The high CO oxidation activity of K_2O/Au(111) depends on the combined contribution from the K-induced reduction in work function and surface accumulation of electron density to activate the oxygen sites, ensemble effect of surface Au sites and electrostatic effect provided by K, which provides active sites to stabilize the C-anchor and O-anchor of CO_2 respectively.[75]

2.3. Cs on Au(111)

The deposition of Cs on Au(111) behaves in a similar way to that of K, demonstrating a coverage-dependent growth mode akin to that observed with KO_x/Au(111) (Fig. 3a).[78] Again, STM captured CsO_x clusters anchored at the herringbone elbows after depositing 0.05 ML on Au(111). The deposited cluster features a Cs : O ratio of ∼1 : 1 and 1.5 Å in height and 2.5 nm in width (Fig. 5a).[78] When the Cs coverage is increased to 0.2 ML (Fig. 5b), 2D islands that contain Cs_2O_2 and a Cs_yO ($y \geq 2$) suboxide emerge. When the coverage of CsO_x is increased to 0.6 ML, the CsO_x islands grow into a continuous film with a rectangular growth pattern (zone A, Fig. 5c) or hexagonal pattern (zone B, Fig. 5c), covering most of Au(111).[78]

The WGS reaction was selected to probe the intrinsic activity of CsO_x/Au(111), where Au(111) alone exhibits negligible reactivity.[79,80] While with coverage less than 0.1 ML, CsO_x-deposited Au(111) effectively dissociates H_2O *via* formation of a Cs–OH bond, which was previously identified as the rate-determining step in the WGS reaction on metal surfaces,[31]

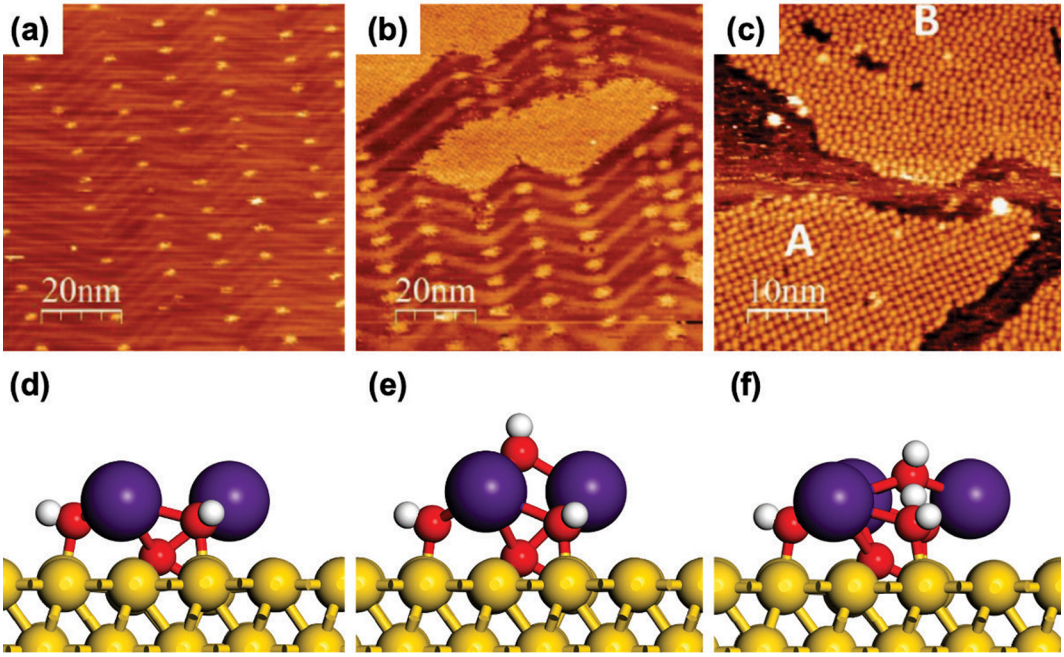

Fig. 5 STM images of CsO_x with different coverages on Au(111): (a) 0.05 ML; (b) 0.2 ML; (c) 0.6 ML. Copyright 2024, American Chemical Society.[78] Side views of DFT-optimized structures for (d) the $Cs_3O_4H_3$/Au(111) model surface with (e) *OH and (f) *H_2O adsorption. Color code: dark purple – Cs; gold – Au; red – O; white – H. Copyright 2023, American Chemical Society.[76]

hereby catalyzing the overall reaction as observed experimentally.[78] The catalytic activity of CsO_x/Au(111) (apparent activation energy: 0.48 eV) is even lower than that on Cu(111) (apparent activation energy: 0.78 eV). To rationalize the Cs promoting effect, the CsO_x clusters at low coverage were described using the $Cs_3O_4H_3$/Au(111) model in DFT calculations, where a Cs : O ratio of 0.75 and coverage of 0.13 ML closely resembled the experimental observations (Fig. 5d). DFT calculations indicated that the deposition of CsO_x destabilizes *OH (Fig. 5e; BE = −2.60 eV *vs.* −2.92 eV, Table 1) but stabilizes H_2O (Fig. 5f; BE = −0.49 eV *vs.* −0.24 eV) with respect to Cu(111). Consequently, *H_2O desorption is effectively hindered, but still enables an exothermic dissociation (reaction energy, ΔE = −0.53 eV) with a low activation barrier (barrier: E_a = 0.13 eV).[76] The preferential hydroxylation of CsO_x clusters weakens the bindings of both *CO and *CO_2 on $Cs_3O_4H_3$/Au(111) (Table 1) and effectively hinders *CO_3 poisoning as seen for KO/Au(111), while it effectively facilitates the oxidation of CO by *OH and the removal of *CO_2. Again, the promoted WGS reaction by Cs decoration is likely associated with the interplay of reduction in work function with the electrostatic effect, which provides selective bond-tuning of reaction intermediates *via* Cs-facilitated and mediated charge transfer from Au(111). Note that Au sites are not involved in the binding directly and the ensemble effect is inhibited in this case.

2.4. Cs on Cu(111)

Different from K/Cu_xO/Cu(111), Cs/Cu_xO/Cu(111) was observed to be unstable and undergo reduction to CsO_x/Cu(111) by annealing at 650 Kelvin as observed by STM (Fig. 6a) and X-ray photoemission spectroscopy (XPS) measurements.[34] According to STM observations, CsO_x nanoclusters are randomly dispersed over Cu(111), which adopts an average of 2 nm in width and ∼1 Å in height. This structural motif is well captured by a triangle $Cs_3O_4H_3$ cluster over Cu(111) (Fig. 6b), where the hydroxylation was also considered to account for the reducing condition of CO_2 hydrogenation.

The introduced $Cs_3O_4H_3$ was found to distinctly stabilize the probing CO_2 molecule (BE = −0.86 eV *vs.* −0.06 eV for Cu), which is more prominent than that of Cs on Au(111) and K on Cu(111) (Table 1). Compared to $Cs_3O_4H_3$/Au(111) and K/Cu_xO/Cu(111), $Cs_3O_4H_3$/Cu(111) has stronger alkali–support interactions and lower-coordinated sites of small clusters with higher fluxionality, respectively. Both factors enable a significant reduction in work function from 5.3 eV to 3.8 eV, Cs-mediated transfer of ∼0.8 electrons and strengthened *CO_2 binding (Table 1). Upon exposure to CO_2, the *OH group of the Cu(111)-supported $Cs_3O_4H_3$ cluster is highly flexible and chemically active forming C–O bonds and *HCO_3 species at the Cs sites (Fig. 6c). In addition, the negatively charged *CO_2 corresponds to a charge accumulation over the O anchor, which provides additional stabilization to the produced *HCO_3 by strengthening the electrostatic $O^{\delta-}$–$Cs^{\delta+}$ interaction (Fig. 6d). Indeed, XPS showed that on exposure to CO_2 the O 1s region of $Cs_3O_4H_3$/Cu(111) was drastically modified and produced a clear feature at ∼531.5 eV corresponding to adsorbed carbonate species.[34]

Overall, the K and Cs metals supported on metal surfaces can be highly sensitive to the exposed environment. Depending on the alkali–support interaction, the coverage and reactive gases exposed, distinct morphologies can be formed, ranging

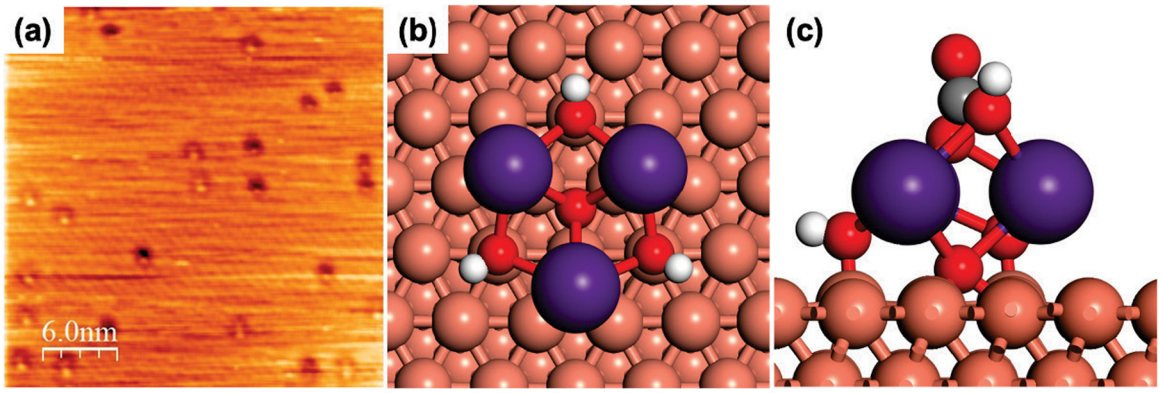

Fig. 6 (a) STM image of CsO_x nanostructures deposited on Cu(111). The CsO_x/Cu(111) surface was prepared by annealing a CsO_x/Cu_2O/Cu(111) system at 650 K. Scanning conditions: 30 nm^2, V_t = 1.25 V, I_t = 0.14 nA. Copyright 2020, AIP Publishing.[34] DFT-optimized structures of (b) $Cs_3O_4H_3$/Cu(111) model surface and (c) *CO_2 on $Cs_3O_4H_3$/Cu(111). Colour code: brown – Cu; dark purple – Cs; red – O; grey – C; white – H. Copyright 2021, American Chemical Society.[66]

from well-dispersed clusters to aggregated islands. Wherein, the presence of alkali always promotes surface oxidation. Such structural variation directly affects the binding properties of the support, where the previously proposed reduction in work function, electronic effect, electrostatic effect and ensemble effect can all contribute. However, how these alkali-induced effects interlay to stabilize CO_2 and likely promote the hydrogenation reaction on Au and Cu surfaces remain elusive. In addition, the alkali-tuned binding can be more complex on moving from CO_2 to other reaction intermediates involved in CO_2 hydrogenation (Fig. 1). To address this complexity and thus the corresponding effect on the overall reaction, an in-depth understanding of the binding nature of alkali-sites is crucial.

3. Selective binding nature of alkalis

In order to understand the nature of K and Cs-introduced bond-tuning, the binding energies of reaction intermediates involved in CO_2 hydrogenation on various surfaces were summarized, including on K/Cu_xO/Cu(111), CsO_x/Cu(111), and CsO_x/Au(111) surfaces (Table 1). Cu(111) was also included for comparison. Note that Cu_xO/Cu(111) was not included, which was reported to undergo reduction to Cu(111) under the reducing condition of CO_2 hydrogenation,[52] while the K deposition promoted the stability *via* strong K–O interaction.[73]

3.1 K/Cu_xO/Cu(111)

On K/Cu_xO/Cu(111), DFT calculations indicated that the K sites are catalytically active and directly interact with the reaction intermediates.[74] Importantly, these interactions are selective, depending on the nature of adsorbate, as clearly demonstrated for *CO_2 and *CO (Fig. 2d and e). Generally, K-induced stabilization is more pronounced for open-shell intermediates, *e.g.*, *HCOO and methoxy (*CH_3O), than closed-shell intermediates, *e.g.*, *HCOOH and *CH_3OH. While the corresponding magnitude varies based on the binding conformation: the adsorbates anchored merely *via* O or O-anchored, such as *HCOO, *H_2COO, *HCOOH, methoxyhydroxy (*H_2COOH), methanediol (*$H_2C(OH)_2$), *CH_2O, *CH_3O, *CH_3OH, *OH and *H_2O along the formate pathway; the adsorbates anchored *via* both O and C or O-/C-co-anchored, such as *CO, *CO_2, *CH_2OH, carboxyl (*COOH) and formyl (*CHO), primarily involved in the RWGS and CO hydrogenation pathways (Fig. 1 and 7).

3.1.1. O-Anchored open-shell intermediates. Among the intermediates considered, *HCOO is stabilized the most by K modification as compared to Cu(111) (BE = −3.75 eV, Table 1). The open-shell –HCOO binds in a bidentate conformation *via* $O^{\delta-}$–$K^{\delta+}$ bonds (Fig. 7b).[73] The adopted C–O bond length (d_{C-O} = 1.27 Å) as well as the O–C–O angle (∠O–C–O = 126.1°) are close to the gas phase $HCOO^-$ ion (d_{C-O} = 1.28 Å, ∠O–C–O = 124.3°).[81,82] Indeed, the Bader charge analysis confirmed a charge transfer of about −0.88*e*, featuring an ionic binding nature. According to the calculated projected density of states (PDOS) and charge density difference, the electron donation to *HCOO is from $Cu^{\delta+}$ at the Cu_xO overlayer and mediated by deposited K (Fig. 8a and b). By comparison, the effect of *HCOO adsorption on Cu^0 is rather small (Fig. 8a). As a result of the K-induced reduction in work function and surface polarization of electron densities, the charge transfer from the surface to *HCOO is facilitated to strengthen the bindings at the K sites. This effect was proposed earlier by Contreras *et al.*[83] and discussed in detail recently for the adsorption process on the oxide surface by Kakekhani *et al.*[84] Without K, *HCOO adopts the same bidentate binding motif on Cu(111) *via* Cu–O bonds; yet the electron transfer is reduced to −0.34*e*, featuring a transition from an ionic to a covalent binding nature. The corresponding binding is weakened to −2.84 eV on Cu(111) (Table 1). Given that, the K-promoted reduction in work function and thus polarization of electron density on the surface likely dominates the stabilization of *HCOO.

Other open-shell O-anchored adsorbates, *i.e.*, *OH, *CH_3O, *H_2COO and *H_2COOH, share the same binding mechanism as *HCOO (Fig. 7). Their interactions with K/Cu_xO/Cu(111) are

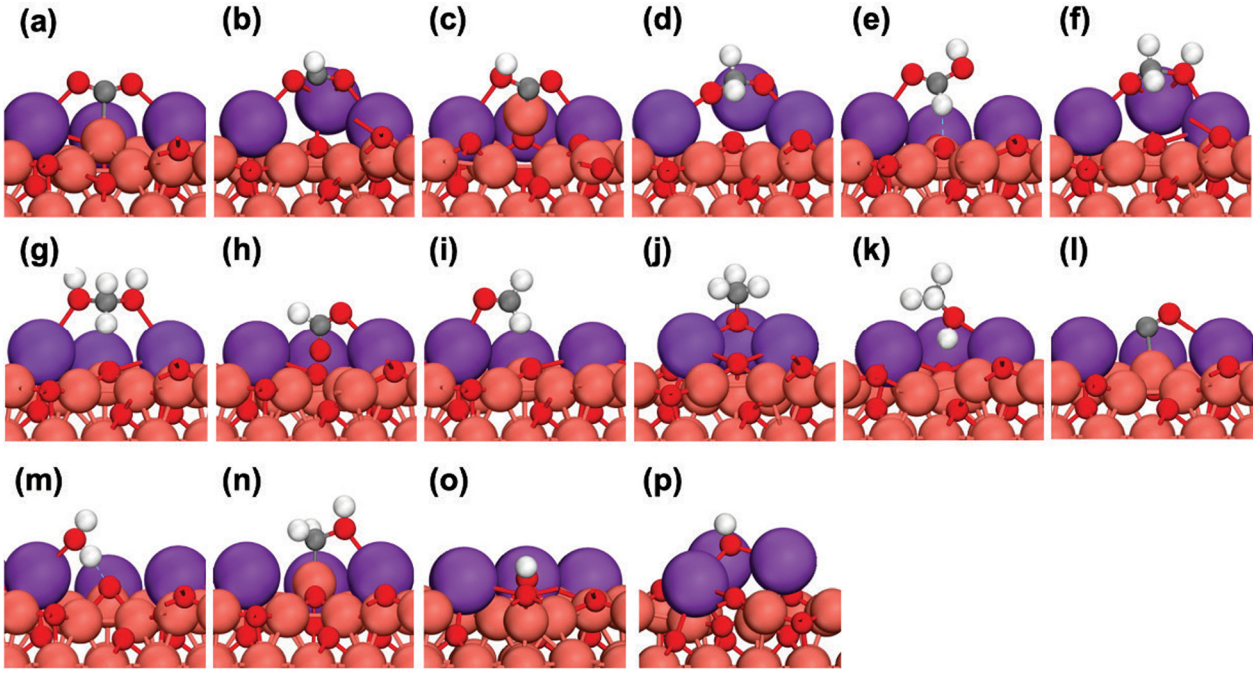

Fig. 7 Side views of the DFT optimized adsorption configurations for selected intermediates on the K/Cu_xO/Cu(111) model surface. (a) *CO_2, (b) *HCOO, (c) *COOH, (d) *H_2COO, (e) *HCOOH, (f) *H_2COOH, (g) *$H_2C(OH)_2$, (h) *CHO, (i) *CH_2O, (j) *CH_3O, (k) *CH_3OH, (l) *CO, (m) *H_2O, (n) *H_2COH, (o) *H, and (p) *OH. Color code: brown – Cu; purple – K; red – O; grey – C; white – H. Copyright 2020, American Chemical Society.[74]

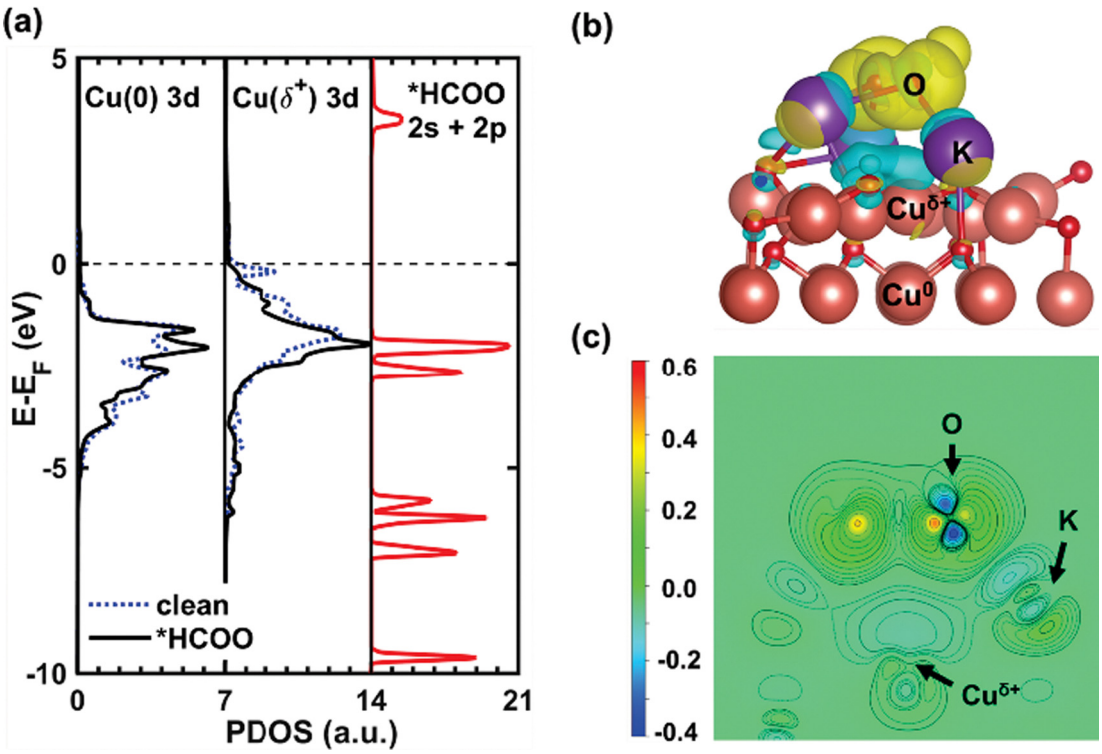

Fig. 8 Electronic structure of *HCOO on K/Cu_xO/Cu(111). (a) Calculated projected density of states (PDOS) for the 3d states of Cu^0 on Cu(111) (left) and $Cu^{\delta+}$ supported Cu_xO layer (middle) before (dashed blue line) and after (solid black line) the adsorption of *HCOO, together with the calculated total DOS of *HCOO (right). (b) Side view of the calculated electron density difference of *HCOO on K/Cu_xO/Cu(111); (c) contour plot of (b), where the cross-section sits on the plane of $Cu^{\delta+}$, K and O. Color code for atoms: brown – Cu; purple – K; red – O; grey – C; white – H. Color code for iso-surfaces: yellow iso-surfaces – charge accumulation; cyan iso-surfaces – charge depletion at 0.001e/a_0^3 (a_0: Bohr radius). Copyright 2020, American Chemical Society.[74]

also strong (BE < -2 eV) and feature an ionic binding nature *via* an electron transfer from the surface to the adsorbate ($\sim -0.8e$). On the other hand, the tuning magnitude by K (ΔBE > -0.5 eV) is not as significant as that of *HCOO (ΔBE = -0.91 eV, Table 1). This reduced impact can be related to factors including the elevated energy of the lowest unoccupied state, elongated K–O bond length, reduced number of oxygen anchors and local structural distortions on interaction.

3.1.2. O-Anchored closed-shell intermediates. In comparison with O-anchored open-shell intermediates, the bindings of closed-shell O-anchored adsorbates, including *HCOOH, *$H_2C(OH)_2$, *CH_2O, *CH_3OH and *H_2O (Fig. 7), correspond to a smaller electron transfer ($\sim -0.1e$), more dominate covalent binding nature, and thus weaker binding (BE = -1.0 to -0.5 eV, Table 1). In this case, the K-mediated charge transfer is limited, while a moderate promoting effect on binding is observed on going from K/Cu_xO/Cu(111) to Cu(111). HCOOH, for example, binds Cu(111) very weakly (BE = -0.24 eV), but gains stability on K/Cu_xO/Cu(111) (BE = -0.84, Table 1) with limited charge transfer ($0.18e$). According to the calculated electron density (Fig. 9), there is no significant charge density for the surface $Cu^{\delta+}$, instead, the formation of O–K bonds *via* the electrostatic $O^{\delta-}$–$K^{\delta+}$ interaction and the HCOO–H$\cdots$$O_{surface}$ hydrogen bond contribute to promoting the stability of *HCOOH.

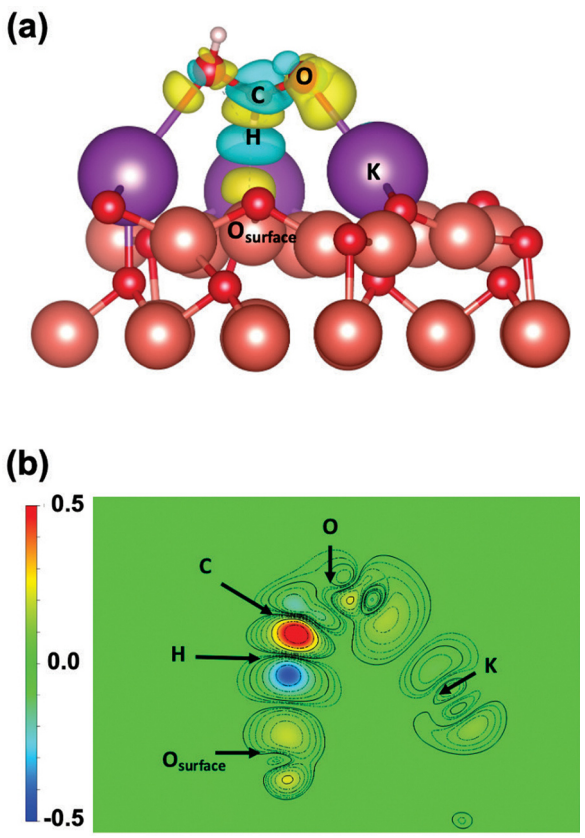

Fig. 9 Structure of *HCOOH on K/Cu_xO/Cu(111). (a) Side view of the calculated electron density difference: yellow and cyan area depict the iso-surface for the accumulation and the depletion of charge density at $0.001e/a_0^3$ (a_0: Bohr radius); (b) contour plot of (a), the cross-section sits on the molecular plane of *HCOOH. Copyright 2020, American Chemical Society.[74]

Similar situations were observed for *H_2O and *CH_3OH with the binding energies strengthened from -0.24 eV and -0.29 eV on Cu(111) to -0.94 eV and -0.85 eV on K/Cu_xO/Cu(111), respectively (Table 1). Again, the electrostatic interactions together with the contribution from hydrogen bonds play a major role, while the contribution due to charge transfer is rather limited ($-0.15e$ and $-0.12e$, respectively). For *$H_2C(OH)_2$ (BE = -0.92 eV *vs.* -0.25 eV for Cu(111), Table 1) and *CH_2O (BE = -0.51 eV *vs.* -0.11 eV for Cu(111), Table 1), although there is a lack of hydrogen bonds, the K-enhanced binding is still maintained, indicating the dominant contribution from the electrostatic stabilization to the oxygen anchors.

3.1.3. C-/O-co-Anchored open-shell intermediates. C-/O-co-anchored open-shell intermediates, such as *COOH, interact with the surface *via* a slightly different mechanism from the O-anchored counterpart, such as *HCOO. While –COOH corresponds to a similar energy level for the lowest unoccupied states (-11.65 eV) as –HCOO (-12.86 eV), a clear reduction in charge transfer from the surface and binding energy is observed on K/Cu_xO/Cu(111) (charge = $-0.47e$ *vs.* $-0.88e$; BE = -2.39 eV *vs.* -3.75 eV, Table 1). This reduction is associated with the transition in binding nature from ionic to covalent interaction, which is demonstrated by a more delocalized charge distribution in *COOH than that of *HCOO (Fig. 8 and 10b, c). Upon adsorption *via* the C–$Cu^{\delta+}$ bond, the valence states of *COOH that consist of π^* states demonstrate a strong resonance with 3d states of $Cu^{\delta+}$ (Fig. 10a). This indicates the dominant role of $(n-1)$ d $\rightarrow \pi^*$ back donation in binding of *COOH, in accordance with the previous report for similar molecules like CO and NO.[85–91] Note that the formation of O–K bonds *via* the electrostatic binding nature also helps, which is less significant than that of C–Cu bonds.

3.1.4. C-/O-co-Anchored closed-shell intermediates. C-/O-co-Anchored closed-shell intermediates such as *CO_2 and *CO also involve the covalent C–$Cu^{\delta+}$ bond and electrostatic $O^{\delta-}$–$K^{\delta+}$ interaction. The presence of a C–Cu covalent bond enables back-donation from the 3d states of $Cu^{\delta+}$ to the π^* states of the adsorbate. However, their closed-shell nature limits the extent of charge transfer from the surface with the elevated energy level of the lowest-unoccupied state (–COOH: -11.65 eV, CO_2: 4.15 eV, CO: 5.05 eV). Nevertheless, the contributions from covalent and electrostatic interactions can effectively activate CO_2 on K/Cu_xO/Cu(111) to form carboxylate-like species (BE = -0.32, Fig. 2 and Table 1), which is a C-/O-co-anchored open-shell intermediate readily able to accept electrons transferred from the surface ($-0.41e$) and transform covalent to ionic binding, while the molecule is only physisorbed on Cu(111) (BE = -0.06 eV, Table 1). This is not the case for *CO, where the closed-shell is maintained on adsorption and the charge transfer ($-0.29e$) is rather limited.[92] The weak covalence of C–$Cu^{\delta+}$ and electrostatic interaction of $O^{\delta-}$–$K^{\delta+}$ results in a weaker binding strength (BE = -0.41 eV, Table 1) than the C–Cu^0 interaction on Cu(111) (BE = -0.89 eV, Table 1).

In general, the deposition of K on Cu(111) and thus the formation of K/Cu_xO/Cu(111) effectively tune the binding of

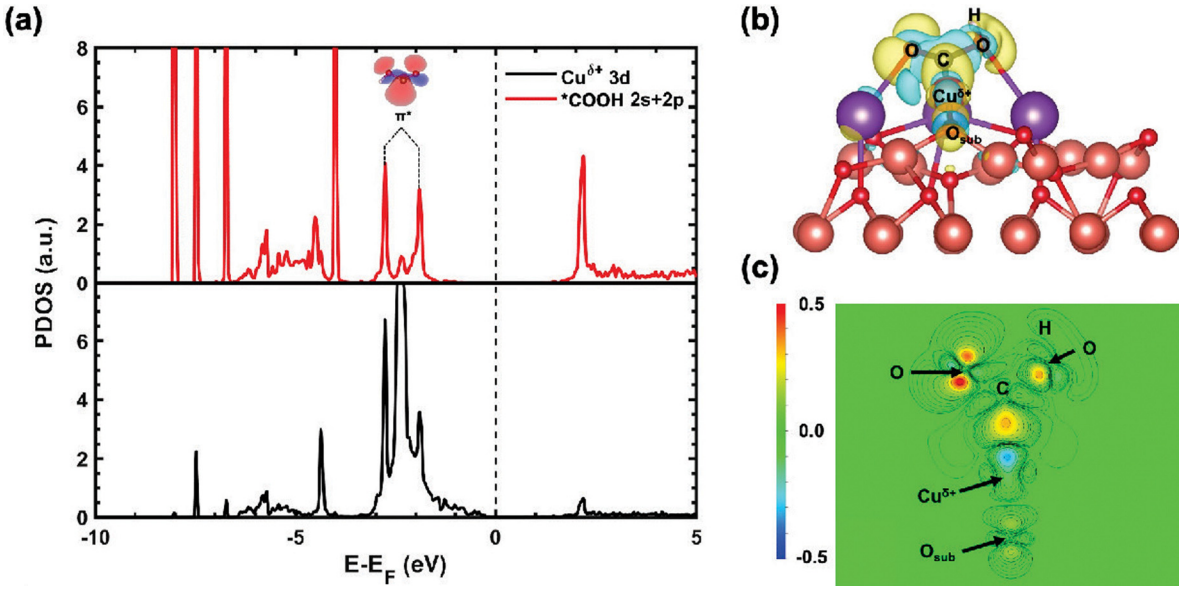

Fig. 10 Structure of *COOH on K/Cu$_x$O/Cu(111). (a) Calculated projected density of states (PDOS) for the 3d states of Cu$^{\delta+}$ (black line) and the interacting *COOH (red line). Inset depicts the calculated wave function of π* states in –COOH(g). (b) Side view of the calculated electron density difference: yellow and cyan areas depict the iso-surface for the accumulation and the depletion of charge density at 0.001e/a_0^3 (a_0: Bohr radius); (c) contour plot of (b), the cross-section sits on the molecular plane of *COOH. Copyright 2020, American Chemical Society.[74]

intermediates involved in CO_2 hydrogenation (Table 1). K participates in the binding directly. Depending on the binding mechanism, the bond-tuning can be divided into three groups. One is the **ionic tuning** that takes advantage of the K-induced reduction in work function and surface accumulation of electron density. It typically results in significant charge transfer and bond-strengthening as seen for O-anchored open-shell intermediates at K sites. Another is the **covalent tuning**, which depends on the ensemble of K and Cu sites and is well demonstrated for adsorptions of the C-/O-co-anchored intermediates. Specifically, the contribution from the surface Cu site is essential to stabilize the C-anchor of adsorbates *via* covalent C–Cu$^{\delta+}$ bonds. Meanwhile, the K site also helps by accommodating the oxygen anchor *via* electrostatic O$^{\delta-}$–K$^{\delta+}$ interaction. Finally, it is the **electrostatic tuning** which benefits the bindings of all intermediates considered *via* O$^{\delta-}$–K$^{\delta+}$ interaction. The intermediates with more O-anchors may form additional K–O bonds to further promote binding. For the intermediates that possess hydroxyl groups, the formation of hydrogen bonding with surface oxygen sites stabilized by K can gain additional stability. Depending on the nature of the intermediates, the contributions from the three types of tunings may vary, thus enabling selective bond-tuning.

3.2. CsO$_x$/Cu(111)

A similar tuning effect to that for K was also observed for Cs deposited on Cu(111) in the form of CsO$_x$/Cu(111) (Table 1).[66] Again, for O-anchored intermediates, the Cs-induced stabilization effect is more prominent for open-shell intermediates *via* the ionic tuning than that on closed-shell intermediates *via* the electrostatic bonding. For example, the bond-strengthening introduced by Cs_3O_4 deposition for open-shell O-anchored *HCOO (ΔBE = −0.66 eV) is more significant than that of closed-shell *HCOOH (ΔBE = −0.17 eV, Fig. 11 and Table 1).

C-/O-co-Anchored intermediates are destabilized on Cs deposition. The origin of Cs-induced destabilization is likely associated with the absence of an ensemble effect at the CsO$_x$–Cu(111) interface. As demonstrated in the case of K/Cu$_x$O/Cu(111), the stabilization of C-/O-co-anchored intermediates requires the participation of Cu sites to form covalent Cu–C bonds. However, the formation of CsO$_x$ clusters on Cu(111) completely blocks the access of adsorbed species at the Cs sites to the surface Cu sites (Fig. 11). The binding of *COOH at the Cs hollow site, for instance, merely depends on the two oxygen anchors *via* electrostatic O$^{\delta-}$–Cs$^{\delta+}$ interactions (Fig. 11). In addition, the charge density in *COOH is accumulated at the dangling C-anchor, likely weakening the electrostatic attraction. As a result, the Cs-decoration does not strengthen the binding of *COOH as seen for K on Cu(111) (ΔBE = −0.73 eV), but results in bond-weakening in this case (ΔBE = 0.13 eV, Table 1).

3.4. CsO$_x$/Au(111)

Upon substituting Cu(111) for Au(111), the local structure of CsO$_x$ remains unchanged (Fig. 5), and the impact on the binding of O-anchored closed-shell intermediates is small.[76] As seen for *HCOOH, the variation in binding energy is only 0.05 eV (Table 1). The stabilization of *HCOOH requires the electrostatic tuning *via* the O$^{\delta-}$–Cs$^{\delta+}$ interaction to be effectively enhanced. However, the DFT results showed the identical charge of Cs and O as well as the same Cs–O distance on Au(111) and Cu(111).[66,76] These results suggest that such electrostatic binding is more sensitive to the local structure of the alkali oxide cluster than the type of substrate.

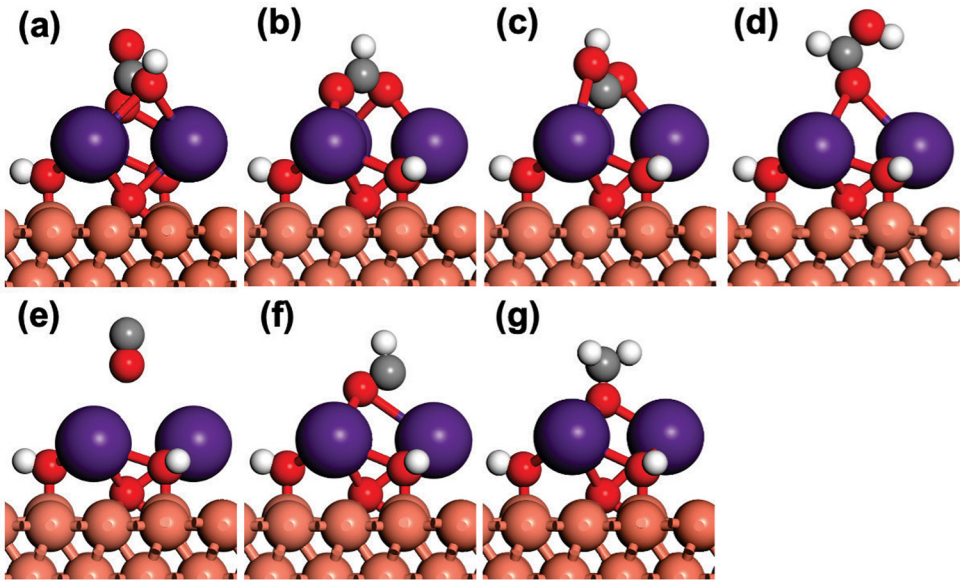

Fig. 11 Side views for DFT optimized structures for selected intermediates in CO_2 hydrogenation on $Cs_3O_4H_3$/Cu(111). (a) *CO_2, (b) *HCOO, (c) *COOH, (d) *HCOOH, (e) *CO, (f) *CHO, and (g) *CH_3O. Color code: brown – Cu; dark purple – Cs; red – O; grey – C; white – H. Copyright 2021, American Chemical Society.[66]

The O-anchored open-shell intermediates behave differently, where the strong binding depends on the Cs-induced ionic tuning. Upon interaction with *HCOO, for example, both Au(111) and Cu(111) transfer approximately one electron to *HCOO, which is mediated by Cs. However, the surface metal sites that interact directly with the CsO_x cluster behave differently. In the case of CsO_x/Cu(111), a drastic downshift in Cu 3d orbital is observed. That is, the adsorption of *HCOO promotes the oxidation of surface Cu, which also helps to lower the corresponding binding energy. By comparison, such downshift is far less profound in Au 5d states. Consequently, *HCOO is more stabilized on the Cs sites when using Cu(111) as the substrate (BE = −3.50 eV) instead of Au(111) (−2.98 eV, Table 1).

The alkali-induced selective binding-tuning to the key reaction intermediates involved in CO_2 hydrogenation can offer a great opportunity to control the operating reaction pathways and the catalytic activity and selectivity. In particular, the preferentially stabilized O-anchored over the C-/O-co-anchored intermediates likely leads to a suppressed RWGS pathway toward CO production but promoting CO_2 activation *via* the formate pathway toward HCOOH or CH_3OH production (Fig. 1 and Table 1). To validate the predictions based on the binding energies of reaction intermediates, detailed studies to map the reaction network and evaluate the catalytic activity and selectivity are necessary.

4. CO_2 hydrogenation at alkali–support interfaces

4.1. K–Cu_xO/Cu(111) interface

Upon depositing K on Cu_xO/Cu(111), $Cu^{\delta+}$ ions were found to remain intact under the reducing condition of CO_2 hydrogenation due to the stabilization of K on interfacial O species, while on Cu_xO/Cu(111) a reduction to Cu^0 was observed.[73,74] As demonstrated below, similar surface oxidation promoted by alkali was also observed for other alkali–support systems. The generated interfaces offer multifunctional centers, including alkali cations, metal cations, and metal and oxygen sites, which can work synergistically to allow selective binding of reaction intermediates and effectively tune the selectivity of CO_2 hydrogenation.

The significantly strengthened K–OOCH bond on K/Cu_xO/Cu(111) promotes the initial CO_2 hydrogenation to *HCOO along the formate pathway according to the DFT-calculated binding energies (Table 1). However, *HCOO may also be overstabilized to suppress the overall conversion. Although the presence of K also helps to stabilize *HCOOH, the effect is not as significant as that for *HCOO (Table 1). In term of selectivity, the K-populated formate pathway can lead to the production of HCOOH and CH_3OH (Fig. 1), which is difficult to predict merely based on the binding energies. A theoretical study was carried out to obtain atomic-level insight into the reaction pathways and kinetics, where the intermediates and transition states along both the formate pathway and the RWGS + CO hydrogenation pathway were taken into consideration.[74]

According to DFT calculations and kinetic Monte Carlo (kMC) simulations under typical experimental conditions (temperature: 400–600 Kelvin; pressure ratio of $CO_2:H_2$ = 1 : 9),[48,50,51,74] the formate pathway was indeed found to dominate the overall CO_2 hydrogenation over K/Cu_xO/Cu(111). The reaction starts with CO_2 adsorption at the K bridge site and is followed by sequential hydrogenations to *HCOO, *HCOOH, *H_2COH, $H_2C(OH)_2$ and eventually *CH_3OH (black line, Fig. 12a). By comparison, the formate pathway *via* *H_2CO (blue line, Fig. 12a) and the RWGS pathway *via* the *COOH

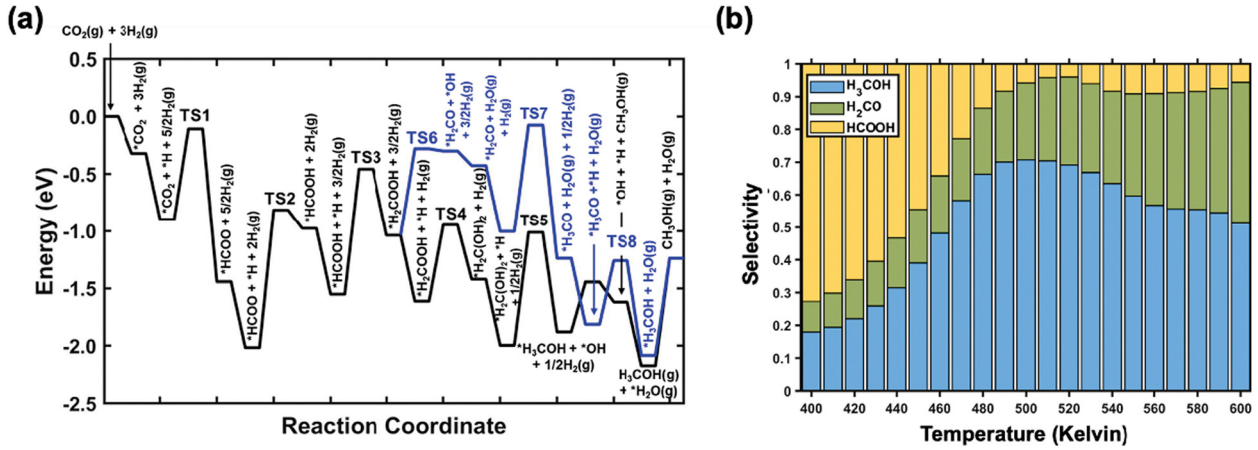

Fig. 12 (a) Potential energy diagrams for the hydrogenation of CO_2 to CH_3OH on the K/Cu_xO/Cu(111) surface including energetics for reaction intermediates and transition states (TS). The blue line indicates the CH_2O-mediated formate pathway, and the black line indicates the $H_2C(OH)_2$-mediated formate pathway. (b) Variation in kMC simulated selectivity for carbon-based products, including CH_3OH (blue), CH_2O (green), and HCOOH (yellow), as a function of temperature during CO_2 hydrogenation over K/Cu_xO/Cu(111). Copyright 2020, American Chemical Society.[74]

intermediate are less competitive. While on the Cu surfaces, it was reported previously that the *H_2CO-mediated formate pathway produces CH_3OH, which is ~2–3 orders of magnitude lower in rate as compared to the CO production *via* the RWGS pathway.[50] In addition, along the RWGS pathway *COOH does not undergo typical C–O bond dissociation,[49,50] but favors hydrogenation to produce *HCOOH, which leads to a merging of the RWGS pathway into the formate pathway. Note that the methanation pathway *via* direct CO_2 dissociation is not preferred on both K/Cu_xO/Cu(111) and Cu surfaces.[74]

Upon exposure of a CO_2/H_2 mixture to K/Cu_xO/Cu(111) ranging from 400 to 600 Kelvin, the kMC simulation observed a variation in selectivity of carbon-based products (Fig. 12b).[74] At 400 Kelvin, the hydrogenation of *HCOOH to H_2COOH is still limited by the high activation barrier (Fig. 12a). Thus, *HCOOH prefers to desorb and HCOOH is the major product (72.6%, Fig. 12b). By comparison, the selectivity to CH_3OH (17.9%) and CH_2O (9.3%) is much lower. Upon going from 400 to 500 Kelvin, the hydrogenation of *HCOOH to H_2COOH and *$H_2C(OH)_2$ is greatly facilitated (black line, Fig. 12a), which lowers the production of HCOOH and maximizes the CH_3OH selectivity (~70.7%). During this process, the CH_2O selectivity also increases from 9.3% to 23.4%. In contrast, the effect on the dissociation of *H_2COOH to *CH_2O (blue line, Fig. 12a), which is a more difficult step, is rather small. With the temperature elevated to 600 Kelvin, the CH_2O selectivity is enhanced the most significantly to 43.0%, which is driven by the increased entropic contribution to *CH_2O desorption. Nevertheless, CH_3OH remains the most selective carbon-based product at 600 Kelvin (49.3%). Notably, the selectivity to CO, which is the major product on Cu,[50] remains as low as 0.3% at the temperatures considered.

The deposited K on Cu_xO/Cu(111) clearly shows the promoting effect on the CO_2 conversion and more importantly tunes the major product from CO as seen for Cu(111) to CH_3OH. During this process, K is not a building block, a simple electron donor or a secondary active site.[10,15,16,42,93] Instead, it is the major active center. According to the sensitivity analysis,[74] reducing the binding strength of O-anchored open-shell *HCOO can effectively promote the CO_2 conversion rate, while stabilizing O-anchored closed-shell *HCOOH is critical to tuning the selectivity toward CH_3OH. The K-induced selective stabilization on *HCOOH *via* the electrostatic $O^{\delta-}$–$K^{\delta+}$ interaction slows down the desorption, so that *HCOOH has a lifetime long enough to be hydrogenated and thus produce CH_3OH (Fig. 9 and 12). However, the ionic tuning by K decoration makes *HCOO too stable to enable facile CO_2 conversion. The fine balance between alkali-induced electrostatic tuning and ionic tuning can be crucial to maximize the selective CO_2 to CH_3OH conversion.

Similar K-promoting effects were also observed for the RWGS reaction over Cu(110), while they were not as prominent as those on Cu(111).[22] Due to the higher-lying Cu d-band center, Cu(110) stabilizes K more significantly than Cu(111), likely hindering the structural fluxionality upon interaction with reaction intermediates. In addition, the work function reduction induced by K adsorption on Cu(110) was also found to be less.[94] As a result, the K-induced bond strengthening of O-containing intermediates was reported to be more significant on Cu(111) than on Cu(110).[22,94]

4.2. CsO_x–Cu(111) interface

Replacing K for Cs on Cu(111) transforms the interface from KO_x–Cu_xO to CsO_x–Cu (Fig. 7 and 11) and the structure of alkali oxide from an overlayer to small clusters, which lead to bond-weakening for most of the reaction intermediates involved in the formate and RWGS pathways (Table 1).[66,74] The CsO_x–Cu(111) interface helps to stabilize *HCOOH and *HCOO at the Cs sites as compared to the Cu sites on Cu(111), although the effect is less pronounced than that observed on K/Cu_xO/Cu(111) (Table 1). Therefore, not only CO_2 conversion, but also methanol selectivity is likely to be improved. This was

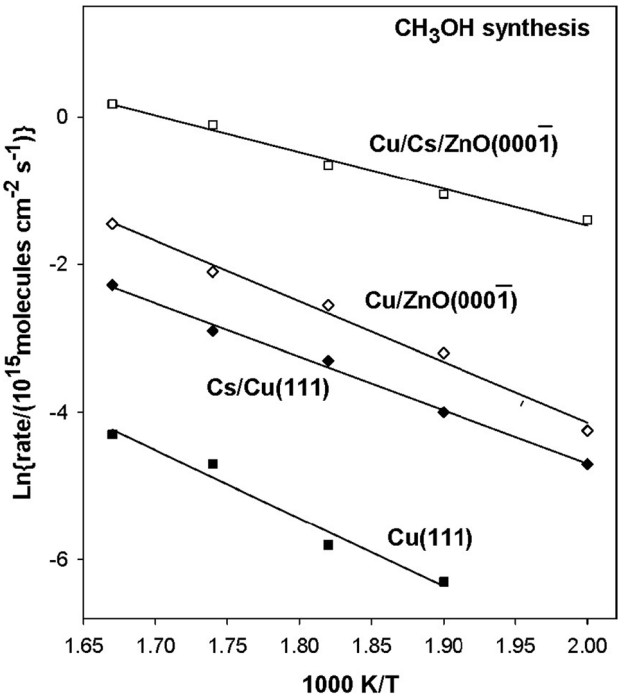

Fig. 13 Arrhenius plot for methanol synthesis on Cu(111), 0.1 ML of Cs on Cu(111), 0.4 ML of Cu on ZnO(000$\bar{1}$), and 0.1 ML Cs on ZnO(000$\bar{1}$) surfaces pre-covered by 0.4 ML of Cu. The catalytic tests were done with 0.049 MPa (0.5 atm) of CO_2 plus 0.441 MPa (4.5 atm) of H_2. Copyright 2021, American Chemical Society.[66]

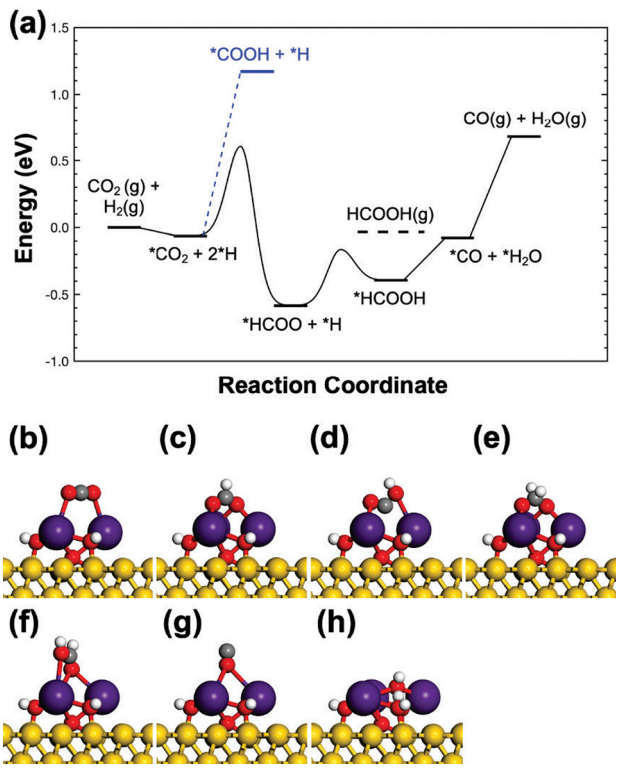

Fig. 14 (a) Potential energy diagram for CO_2 hydrogenation on the $Cs_3O_4H_3$/Au(111) surface. Front views of DFT optimized adsorption configurations for the selected intermediates: (b) *CO_2, (c) *HCOO, (d) *COOH, (e) *H_2COO, (f) *HCOOH, (g) *CO, and (h) *H_2O. Color code: gold – Au; dark purple – Cs; red – O; grey – C; white – H. Copyright 2023, American Chemical Society.[76]

confirmed by an experimental study, where CsO_x/Cu(111) was identified as the active phase of CsO_x/Cu_xO/Cu(111) under 0.5 atm CO_2 and 4.5 atm H_2, able to produce CH_3OH 10 times faster than that on Cu(111) (Fig. 13).[66] The difference in CO_2 hydrogenation between K and Cs modification on Cu remains elusive. According to the DFT calculations (Table 1), instead, compared to K/Cu_xO/Cu(111), the destabilized *HCOO by CsO_x/Cu(111) may facilitate the CO_2 conversion, but the weakened *HCOOH binding may reduce the selectivity of CH_3OH. However, this prediction still needs to be validated by performing a direct comparison of catalytic performance based on theoretical calculations and experimental studies.

4.3. CsO_x–Au(111) interface

Moving from Cu(111) to Au(111) destabilizes all reaction intermediates in the Cs sites at the interface (Table 1). Yet, the bindings of *HCOO and *HCOOH are still more stable than on Cu(111). Thus, the enhanced CO_2 conversion *via* the formate pathway and selective production of CH_3OH are expected, which was validated experimentally. Herein, the activation of CO_2 over CsO_x/Au(111) was observed even at room temperature, which is not feasible on Cu(111).[49,50,76] However, only HCOOH is produced.

According to the DFT calculations, indeed the RWGS pathway *via* the *COOH intermediate cannot compete with the formate pathway as observed for K-modified Cu_xO/Cu(111) (Fig. 14a).[74,76] With the suppressed contribution of charge transfer into the bindings of the open-shell intermediates, the initial hydrogenation of *CO_2 into *COOH is even more endothermic on CsO_x/Au(111) than that on CsO_x/Cu(111), by 0.28 eV, though the same adsorption conformation is adopted (Fig. 14b). Instead, the formate pathway is more preferred. Due to the selective destabilization of *HCOO over *HCOOH on going from Cu(111) to Au(111), the hydrogenation from *HCOO to *HCOOH is greatly facilitated on CsO_x/Au(111), corresponding to a reduced reaction energy from 1.10 eV to 0.14 eV along with a low activation barrier of 0.42 eV (Fig. 14a). In this case, *HCOOH is stable enough to allow *HCOO hydrogenation. However, it is not ready for the further hydrogenation and decomposition to produce CH_3OH, instead overcoming a 0.36 eV barrier for facile desorption.

4.4. Cs–Cu–ZnO(000$\bar{1}$) interface

The tri-phase interface of Cs–Cu–ZnO(000$\bar{1}$) offers a distinct opportunity to take advantage of the ensemble effect among alkali, metal and metal oxide sites as compared to the dual-phase interfaces, alkali–metal and alkali–oxide, as demonstrated above. A gradual increase in the production of CH_3OH from CO_2 hydrogenation when going from Cu(111), CsO_x/Cu(111), Cu/ZnO(000$\bar{1}$) to Cs/Cu/ZnO(000$\bar{1}$) was observed experimentally under 0.5 atm of CO_2 and 4.5 atm of H_2 (Fig. 13).[66] This promoting effect was well captured by the DFT-based kMC simulations. The results showed that under the same condition the average rate for CH_3OH

synthesis on Cu/ZnO(000$\bar{1}$) was increased by about four orders of magnitude by the Cs decoration, in reasonable agreement with the experimentally measured increase of about two orders of magnitude (Fig. 13).[66]

According to the kMC analysis, under these reaction conditions the CO_2 hydrogenation undergoes *via* both the formate pathway and RWGS + CO hydrogenation pathway, which leads to *CHO and eventually *CH_3OH formations on Cs/Cu/ZnO(000$\bar{1}$) (Fig. 15a and b).[66] Herein, the Cs–Cu–ZnO(000$\bar{1}$) interface was identified as the active sites (Fig. 15c–j). The introduction of Cu nanoparticles and thus the low-coordinated Cu sites can greatly enhance the binding properties compared with the Cu sites on the Cu_xO layer and Cu(111) as reported previously.[50,51,74] Given this, the ensemble effect to stabilize the C-anchors of reaction intermediates can be advanced. Meanwhile, the nearby Cs sites also help to interact with the O-anchor as seen for other alkali-decorated systems.[66] The ensemble effect *via* the synergy between Cs and Cu at the Cs–Cu–ZnO(000$\bar{1}$) interface significantly strengthens the binding of C-/O-co-anchored intermediates, *e.g.* *CO_2, *COOH, *CO and *CHO, which are involved in the RWGS + CO hydrogenation pathway (Fig. 15a and Table 2).[66] As a result, CO_2 can be activated to form carboxylate-like species, which allows an additional contribution from the ionic tuning to strengthen the binding by 1.19 eV as compared to CsO_x/Cu(111) and 1.45 eV as compared to Cu/ZnO(000$\bar{1}$) (Fig. 15c and Table 2). The kMC results confirmed that the stabilized *CO_2 at the interface promotes CO_2 conversion to *CHO and to CH_3OH. Similar promoting behaviors were also observed for *COOH, *CHO and *CO (Table 2).

Compared to the C-/O-co-anchored intermediates, stabilization of the O-anchored intermediates at the Cs–Cu–ZnO interface is generally less significant (Table 2). Although *HCOO is anchored at the interface *via* both O–Cs and O–Cu bonds (Fig. 15d), the missing Cu–C bond limits the contribution from the covalent tuning and the corresponding binding is only stabilized by 0.42 eV compared to Cu/ZnO(000$\bar{1}$) (Table 2). Yet, an increase in binding of 1.66 eV is gained as compared to CsO_x/Cu(111), demonstrating the significant contribution from low-coordinated Cu sites. *HCOOH is adsorbed at the interface in a similar configuration as that of *HCOO, however, in addition to O–Cs and O–Cu bonds, a hydrogen bond is formed with ZnO(000$\bar{1}$), which results in a stronger binding than that of Cu/ZnO(000$\bar{1}$) and CsO_x/Cu(111) (Fig. 15e and Table 1).

Due to selective bond-strengthening of C-/O-co-anchored intermediates over O-anchored intermediates at the Cs–Cu–ZnO(000$\bar{1}$) interface, the formate and RWGS + CO hydrogenation pathways are competitive in producing *CHO according to the kMC simulation.[66] While the formate pathway is highly preferred for the single phase, Cu, and dual-phase interfaces, K–Cu_xO, Cs–Cu, K–Au, Cs–Au and Cu–ZnO. In particular, the stability of *CHO is fine-tuned on Cs/Cu/ZnO(000$\bar{1}$). It is stable enough to drive the C–O bond scission of *HCOOH and prevent the further decomposition to CO, which has been observed for Cu-based systems,[50,51,95] but weak enough to be readily available for hydrogenation to produce CH_3OH (Fig. 15a and b). More importantly, the appropriate tuning for *CHO at the

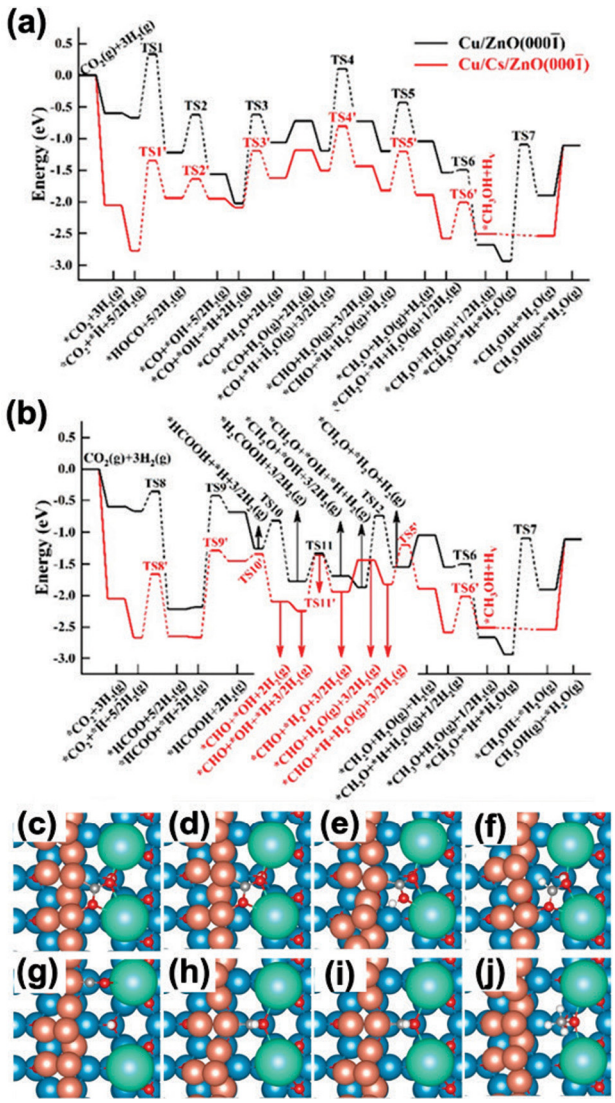

Fig. 15 Potential energy diagram for CH_3OH synthesis from CO_2 hydrogenation on Cu/ZnO(000$\bar{1}$) (black lines) and Cs/Cu/ZnO(000$\bar{1}$) (red lines) *via* the (a) RWGS + CO hydrogenation pathway and (b) formate pathway. Top views of the DFT optimized structures of selected key intermediates: (c) *CO_2, (d) *HCOO, (e) *COOH, (f) *HCOOH, (g) *CO, (h) *CHO, (i) *CH_2O, and (j) *CH_3O. Color code: blue – Zn; brown – Cu; green – Cs; grey – C; white – H. Copyright 2021, American Chemical Society.[66]

Table 2 DFT calculated binding energy (BE) comparison for the selected species on Cu/ZnO(000$\bar{1}$), CsO_x/Cu(111), and Cs/Cu/ZnO(000$\bar{1}$) surfaces[66]

	BE (eV)		
Species	Cu/ZnO(000$\bar{1}$)	$Cs_3O_4H_3$/Cu(111)	Cs/Cu/ZnO(000$\bar{1}$)
*CO_2	−0.60	−0.86	−2.05
*HCOO	−4.74	−3.50	−5.16
*COOH	−3.52	−1.73	−4.23
*HCOOH	−0.72	−0.41	−1.49
*CO	−1.45	−0.17	−1.93
*CHO	−2.57	−0.73	−3.28

Cs–Cu–ZnO(000$\bar{1}$) interface was also found to enable the formation of OHC*–*CHO pairs and facilitate the C–C coupling to produce C_2H_5OH, though the C_2H_5OH selectivity is much lower than that of CH_3OH.[66]

5. Summary and outlook

Recent advancements in surface science and theoretical studies of model catalysts have contributed to an in-depth understanding of the morphology of alkali–support interfaces, the selective binding nature of alkali sites, and rational tuning of catalytic activity and selectivity by alkali promoters. This review clearly demonstrates that the variation in combination and local atomic arrangement of alkali (K, Cs) – metal (Cu, Au) or metal oxide (Cu_xO, ZnO) interfaces under CO_2 hydrogenation conditions can effectively facilitate the conversion and selectivity towards various value-added chemicals: formic acid, methanol, and ethanol.

The morphology of K, Cs–Cu(111), and Au(111) interfaces strongly depends on alkali–support interactions, coverages, and reactive environments, ranging from dispersed clusters to aggregated islands.[34,76,78,96] The role of an alkali is multifunctional, as it promotes surface oxidation, reduces work function, induces polarization of electron densities to the surface, and thus tunes the binding of adsorbates *via* facilitated charge transfer from the surface, electrostatic interactions and synergy with nearby sites at the interfaces.[34,74,76] As a result, the alkali-induced bond-tuning is selective to the reaction intermediates involved in CO_2 hydrogenation *via* three mechanisms: (1) ionic tuning, which leverages alkali-induced reductions in work function and accumulations of surface electron density to particularly stabilize O-anchored open-shell intermediates at alkali sites; (2) covalent tuning, which is reliant on the ensemble effect between alkali and metal sites at the interface to interact with C-/O-co-anchored intermediates; (3) electrostatic tuning, which benefits all intermediates by enhancing $O^{\delta-}$–$K/Cs^{\delta+}$ interactions.[66,74,76]

Moving from Cs–Cu(111) to K–Cu(111) interface introduces covalent tuning, which interacts with the ionic and electrostatic tunings at the K–Cu_xO/Cu(111) interface to enhance CO_2 activation and methanol production along the alkali-populated formate pathway. However, the destabilized open-shell *HCOO helps alleviate surface poisoning, and the stabilized closed-shell *HCOOH enhances selective CO_2 conversion to CH_3OH.[66,74] Adjusting the substrate from Cu(111) to Au(111) limits ionic tuning and electrostatic tuning and results in destabilized *HCOOH and *HCOO, while covalent tuning remains inhibited. Consequently, CsO_x/Au(111) selectively produces HCOOH from CO_2 rather than CH_3OH, suggesting the critical role of covalent tuning in selective conversion to alcohols.[76] Indeed, the Cs–Cu–ZnO(000$\bar{1}$) interface significantly enhances CH_3OH turnover frequency compared to CsO_x/Cu(111) by providing the low-coordinated Cu sites from Cu nanoparticles to enhance covalent tuning. In particular, the binding of *CHO can be tuned sufficiently, not only to facilitate the decomposition of *HCOOH and sequential hydrogenation to CH_3OH, but also to initiate C–C coupling and ethanol C_2H_5OH.[66]

Despite the advances on well-defined model surfaces, insight into the alkali-tuning effect for CO_2 hydrogenation over practical powder catalysts remains limited, though the impact is significant. So far, different alkali-induced tuning effects have been proposed. Depositing alkali metals on Co_2C/SiO_2,[97] Ni/CeO_2,[98] Cu/SiO_2,[67] Pt/mullite,[33] and Rh_1/ZrO_2[99] was shown to modify the binding properties of the support and enhance metal dispersion or mitigate sintering, thereby increasing CO_2 conversion. In addition, introducing K was reported to reduce the specific surface area and the number of exposed active sites over Cu/SiO_2,[67] $CoCu/TiO_2$,[27] Co/ZrO_2,[100] Ni/CeO_2,[98] Ni/Al_2O_3,[101] Co/Al_2O_3,[102] CuO/CeO_2,[26] and Zr–Co/anatase-TiO_2,[97] lowering the activity, while the impact on selectivity was less addressed. Significant selectivity-tuning by alkalis was observed for supported Cu catalysts, being able to completely suppress methanol synthesis but produce CO *via* the RWGS reaction.[67] However, for Fischer–Tropsch catalysts such as Co/Al_2O_3,[102] $CoCu/TiO_2$,[27] Co_2C/SiO_2,[97] $(Co_3O_4 + Co_2C)@Co^0$,[103] Fe/C,[104] and $Fe_3O_4@(Fe_5C_2 + Fe_3O_4)$,[105] the formation of C_{2+} products from CO_2 hydrogenation, including long-chain hydrocarbons and higher alcohols, is promoted by alkalis. Nevertheless, the underlying mechanisms in all cases remain elusive. Efforts along the following aspects are imperative to enhance the complexity of current model studies, gradually building the atomic understanding of behaviors of alkali-decorated powder catalysts under reaction conditions and advancing the practical application of alkali promoters in CO_2 hydrogenation:

(1) Bridging pressure gap to describe interactions between model alkali–support interfaces and reaction conditions. The majority of theoretical studies primarily described the interface by simply depositing alkali on the support, *e.g.*, Ni(111),[18] Rh(111),[20] Au(111),[106] PdPt(111),[107] FeO(100),[108] MoP(001),[109] MoS_2(100)[110] and Pt/TiO_2(110).[111] However, these models often lack sufficient fidelity to capture the diversity of alkali morphologies on interaction with the reactive environment. Recently, a computational framework was developed that is capable of accurately predicting activity and selectivity of Pd-based catalysts during CO_2 hydrogenation by explicitly accounting for the effect of reaction pressure and temperature on catalyst surface structure and dynamics.[112] Herein, the structures of the as-prepared and spent catalysts are different from those during reaction, which are relevant to catalysis. Similar studies will help to map the diverse surface configurations under relevant conditions, which have been demonstrated to effectively impact the alkali-tuned binding to reaction intermediates and thus the catalytic behaviors. Besides, the coordinated *in situ* characterization on the structures and binding properties of alkali-modified model surfaces is essential to ensure the precision of theoretical prediction on surface structures, which can differ significantly from the *ex situ* characterization.[113–117]

(2) Bridging the material gap to capture the structural complexity of powder catalysts. Even though the well-characterized model surfaces can improve the mechanistic understanding of alkali-induced catalytic tuning, in some cases the

models are not complex enough to capture the catalytic behaviors of practical power catalysts. For instance, the model study of CO_2 hydrogenation over K-modified Cu(111) suggested selective CH_3OH synthesis *via* the promoted formate pathway, with suppression of the RWGS reaction.[74] However, the results for K-modified Cu/SiO_2 powder catalysts showed selective CO production *via* a promoted RWGS reaction.[67,118–120] Although both systems involve surface oxidation of Cu and the formation of a K–Cu_xO interface,[120] the model surface may not adequately mimic the details such as the local K coverage, the low-coordinated Cu sites of Cu nanoparticles and their preferential motif in interaction with the support and K, thus limiting the capability of model studies to aid in the understanding of power catalysts. Indeed, upon going from Cs/Cu(111) to Cs/Cu/ZnO(000$\bar{1}$), as demonstrated, not only significant improvement in CO_2 conversion to methanol, but also the emerging of ethanol production was observed by including the effect of support and nanoscale Cu catalysts.[66] Given that, the complexity of model catalysts needs to be further enhanced to reduce the gap with powder catalysts, which can potentially facilitate the design of alkali-modified catalysts.

(3) Controlling synthesis to ensure coordination of multiple active sites at interfaces. Morphology control of particles is important in heterogeneous catalysis by changing the crystallographic orientation and providing diverse atomic arrangements and active sites.[121–124] The stabilized *CHO on Cs/Cu/ZnO(000$\bar{1}$), for example, enabled the C–C coupling with low C_2H_5OH production from CO_2 on combination of Cs sites and Cu nanoparticles.[66] By reducing the size of Cu particles with a MOF structure, Cs/Z_{12}-bpdc-Cu, the combination of Cs and Cu_2 centers was found to be highly selective for CO_2 hydrogenation to C_2H_5OH with >99% selectivity.[125] Besides the size and shape of metal or metal oxide particles, controlling the loading of alkali and its relative position with respect to the adjacent sites should also be considered, which can impose additional tuning effects to the bindings of reaction intermediates. Ideally, the alkali–support interface should be arranged in a way that maximizes the interplay among ionic, covalent and electrostatic tunings to optimize catalytic activity and selectivity.

(4) Evaluating stability. Due to the ionic tuning effect, the deposition of alkali metal tends to interact strongly with the O-anchored open-shell intermediates, such as *HCOO and *CO_3 species in CO/CO_2 hydrogenations, *via* significant surface-to-adsorbate charge transfer and thus strong O–K/Cs interactions. Experimentally, both *HCOO and *CO_3 species are frequently observed on alkali-modified catalysts as abundant surface species.[26,33,126–132] Such strong binding at the alkali sites can help to facilitate the adsorption of CO_2 and thus overall CO_2 conversion, while in some cases these species are over-stabilized and form a self-assembled K/Cs^+–CO_3^{2-} or K/Cs^+–$HCOO^-$ island, which block or decompose the active sites at the interface.[15] To avoid such potential problems, kinetic studies including the multiple pathways running in parallel are necessary, making sure that catalyst deactivation over time does not occur under the reaction conditions. The theoretical kinetic studies should also be supplemented by a long-term stability test to determine the stability of alkali promoters under reaction temperatures and pressures.[133]

Data availability

No primary research results, software or code were included and no new data were generated or analyzed as part of this review.

Conflicts of interest

The authors declare no conflicts of interest.

Acknowledgements

The authors acknowledge the financial support provided by the Chemical Sciences, Geosciences, and Biosciences Division, Office of Basic Energy Science of the US Department of Energy (DOE) under contract no. DE-SC0012704 through BNL-FWP CO-040.

References

1 M. Luo, R. J. O'Brien, S. Bao and B. H. Davis, *Appl. Catal., A*, 2003, **239**, 111–120.
2 K. Liu, A. Wang and T. Zhang, *ACS Catal.*, 2012, **2**, 1165–1178.
3 M. Yang, J. Liu, S. Lee, B. Zugic, J. Huang, L. F. Allard and M. Flytzani-Stephanopoulos, *J. Am. Chem. Soc.*, 2015, **137**, 3470–3473.
4 G. Preda, G. Pacchioni, M. Chiesa and E. Giamello, *Phys. Chem. Chem. Phys.*, 2009, **11**, 8156–8164.
5 D. O. Uner, *Ind. Eng. Chem. Res.*, 1998, **37**, 2239–2245.
6 G. Ertl, M. Weiss and S. B. Lee, *Chem. Phys. Lett.*, 1979, **60**, 391–394.
7 Q. Wang, J. Guo and P. Chen, *Chem*, 2021, **7**, 3203–3220.
8 A. Ozaki, *Acc. Chem. Res.*, 1981, **14**, 16–21.
9 J. H. Pazmiño, M. Shekhar, W. Damion Williams, M. Cem Akatay, J. T. Miller, W. Nicholas Delgass and F. H. Ribeiro, *J. Catal.*, 2012, **286**, 279–286.
10 P. Panagiotopoulou, *Appl. Catal., B*, 2018, **236**, 162–170.
11 T. Wu, J. Lin, Y. Cheng, J. Tian, S. Wang, S. Xie, Y. Pei, S. Yan, M. Qiao, H. Xu and B. Zong, *ACS Appl. Mater. Interfaces*, 2018, **10**, 23439–23443.
12 B. Liang, H. Duan, T. Sun, J. Ma, X. Liu, J. Xu, X. Su, Y. Huang and T. Zhang, *ACS Sustainable Chem. Eng.*, 2019, **7**, 925–932.
13 J. A. Rodriguez, E. R. Remensal, P. J. Ramirez, I. Orozco, Z. Liu, J. Graciani, S. D. Senanayake and J. Fernández Sanz, *ACS Catal.*, 2019, **9**, 10.
14 N. Fischer, R. Henkel, B. Hettel, M. Iglesias, G. Schaub and M. Claeys, *Catal. Lett.*, 2016, **146**, 509–517.
15 I. Waluyo, K. Mudiyanselage, F. Xu, W. An, P. Liu, J. A. Boscoboinik, J. A. Rodriguez and D. J. Stacchiola, *J. Phys. Chem. C*, 2019, **123**, 8057–8066.

16 J. Ren, Y. Wang, J. Zhao, S. Tan and H. Petek, *J. Am. Chem. Soc.*, 2019, **141**, 4438–4444.
17 B. A. Rohr, A. R. Singh and J. K. Nørskov, *J. Catal.*, 2019, **372**, 33–38.
18 M. Zhou and B. Liu, *ChemCatChem*, 2015, **7**, 3928–3935.
19 F. Zasada, P. Stelmachowski, G. Maniak, J.-F. Paul, A. Kotarba and Z. Sojka, *Catal. Lett.*, 2009, **127**, 126–131.
20 N. Yang, X. Liu, A. S. Asundi, J. K. Nørskov and S. F. Bent, *Catal. Lett.*, 2018, **148**, 289–297.
21 Y.-X. Wang and G.-C. Wang, *Phys. Chem. Chem. Phys.*, 2018, **20**, 19850–19859.
22 Y.-X. Wang and G.-C. Wang, *ACS Catal.*, 2019, **9**, 2261–2274.
23 C. Liu and P. Liu, *ACS Catal.*, 2015, **5**, 1004–1012.
24 Y.-X. Wang and G.-C. Wang, *J. Phys. Chem. C*, 2018, **122**, 15474–15484.
25 B. Zhao and G.-C. Wang, *J. Phys. Chem. C*, 2019, **123**, 17273–17282.
26 G. Varvoutis, M. Lykaki, E. Papista, S. A. C. Carabineiro, A. C. Psarras, G. E. Marnellos and M. Konsolakis, *J. CO_2 Util.*, 2021, **44**, 101408.
27 Z. Shi, H. Yang, P. Gao, X. Chen, H. Liu, L. Zhong, H. Wang, W. Wei and Y. Sun, *Chin. J. Catal.*, 2018, **39**, 1294–1302.
28 R. Shi, W. Liao, P. J. Ramírez, I. Orozco, M. Mahapatra, J. Kang, A. Hunt, I. Waluyo, S. D. Senanayake, P. Liu and J. A. Rodriguez, *Angew. Chem., Int. Ed.*, 2022, **61**, e202208666.
29 Y.-Y. Song and G.-C. Wang, *Catal. Sci. Technol.*, 2022, **12**, 1487–1498.
30 M. M. Rodriguez, E. Bill, W. W. Brennessel and P. L. Holland, *Science*, 2011, **334**, 780–783.
31 C. T. Campbell and B. E. Koel, *Surf. Sci.*, 1987, **186**, 393–411.
32 J. A. Rodriguez, E. R. Remesal, P. J. Ramírez, I. Orozco, Z. Liu, J. Graciani, S. D. Senanayake and J. F. Sanz, *ACS Catal.*, 2019, **9**, 10751–10760.
33 B. Liang, H. Duan, X. Su, X. Chen, Y. Huang, X. Chen, J. J. Delgado and T. Zhang, *Catal. Today*, 2017, **281**, 319–326.
34 R. Hamlyn, M. Mahapatra, I. Orozco, A. Hunt, I. Waluyo, M. G. White, S. D. Senanayake and J. Rodriguez, *J. Chem. Phys.*, 2020, **152**, 044701.
35 R. M. Liu, C. M. Chen, W. Chu and W. J. Sun, *Materials*, 2022, **15**, 13.
36 R. W. Gurney, *Phys. Rev.*, 1935, **47**, 479–482.
37 J. P. Muscat and D. M. Newns, *Surf. Sci.*, 1978, **74**, 355–364.
38 N. D. Lang, *Phys. Rev. B: Condens. Matter Mater. Phys.*, 1971, **4**, 4234–4244.
39 F. M. Hoffmann and R. A. de Paola, *Phys. Rev. Lett.*, 1984, **52**, 1697–1700.
40 H. P. Bonzel, *Surf. Sci. Rep.*, 1988, **8**, 43–125.
41 H. Li, T. Chen and G. Wang, *Appl. Catal., A*, 2022, **639**, 118607.
42 L. Proaño, E. Tello, M. A. Arellano-Trevino, S. Wang, R. J. Farrauto and M. Cobo, *Appl. Surf. Sci.*, 2019, **479**, 25–30.
43 L. Lopez, V. Montes, H. Kušar, S. Cabrera, M. Boutonnet and S. Järås, *Appl. Catal., A*, 2016, **526**, 77–83.
44 A. M. Hilmen, M. T. Xu, M. J. L. Gines and E. Iglesia, *Appl. Catal., A*, 1998, **169**, 355–372.
45 C. Zhang, S. Li, L. Zhong and Y. Sun, *J. Phys. Chem. C*, 2021, **125**, 6061–6072.
46 K. C. Waugh, *Catal. Today*, 1992, **15**, 51–75.
47 M. Behrens, F. Studt, I. Kasatkin, S. Kühl, M. Hävecker, F. Abild-Pedersen, S. Zander, F. Girgsdies, P. Kurr, B.-L. Kniep, M. Tovar, R. W. Fischer, J. K. Nørskov and R. Schlögl, *Science*, 2012, **336**, 5.
48 S. Kattel, P. J. Ramírez, J. G. Chen, J. A. Rodriguez and P. Liu, *Science*, 2017, **355**, 1296–1299.
49 L. C. Grabow and M. Mavrikakis, *ACS Catal.*, 2011, **1**, 365–384.
50 Y. Yang, J. Evans, J. A. Rodriguez, M. G. White and P. Liu, *Phys. Chem. Chem. Phys.*, 2010, **12**, 9909–9917.
51 Y. Yang, M. G. White and P. Liu, *J. Phys. Chem. C*, 2012, **116**, 248–256.
52 J. Graciani, K. Mudiyanselage, F. Xu, A. E. Baber, J. Evans, S. D. Senanayake, D. J. Stacchiola, P. Liu, J. Hrbek, J. F. Sanz and J. A. Rodriguez, *Science*, 2014, **345**, 546.
53 S. Kattel, B. Yan, Y. Yang, J. G. Chen and P. Liu, *J. Am. Chem. Soc.*, 2016, **138**, 12440–12450.
54 J. Ye, C. Liu, D. Mei and Q. Ge, *ACS Catal.*, 2013, **3**, 1296–1306.
55 J. Wang, G. Zhang, J. Zhu, X. Zhang, F. Ding, A. Zhang, X. Guo and C. Song, *ACS Catal.*, 2021, **11**, 1406–1423.
56 W. Liao, C. Tang, H. Zheng, J. Ding, K. Zhang, H. Wang, J. Lu, W. Huang and Z. Zhang, *J. Catal.*, 2022, **407**, 126–140.
57 J. Nunan, K. Klier, C.-W. Young, P. B. Himelfarb and R. G. Herman, *J. Chem. Soc., Chem. Commun.*, 1986, 193–195, DOI: 10.1039/C39860000193.
58 J. A. Rodriguez, W. D. Clendening and C. T. Campbell, *J. Phys. Chem.*, 1989, **93**, 5238–5248.
59 J. A. Rodriguez, W. D. Clendening, J. M. Campbell, W. Min and C. T. Campbell, *J. Vac. Sci. Technol., A*, 1989, **7**, 2118–2120.
60 J. Nakamura, J. M. Campbell and C. T. Campbell, *J. Chem. Soc., Faraday Trans.*, 1990, **86**, 2725–2734.
61 K. Klier, R. G. Herman, J. G. Nunan, K. J. Smith, C. E. Bogdan, C. W. Young and J. G. Santiesteban, in *Stud. Surf. Sci. Catal.*, ed. D. M. Bibby, C. D. Chang, R. F. Howe and S. Yurchak, Elsevier, 1988, vol. 36, pp. 109–125.
62 J. G. Nunan, C. E. Bogdan, K. Klier, K. J. Smith, C.-W. Young and R. G. Herman, *J. Catal.*, 1988, **113**, 410–433.
63 J. Sun, S. Wan, F. Wang, J. Lin and Y. Wang, *Ind. Eng. Chem. Res.*, 2015, **54**, 7841–7851.
64 J. Sun, Q. Cai, Y. Wan, S. Wan, L. Wang, J. Lin, D. Mei and Y. Wang, *ACS Catal.*, 2016, **6**, 5771–5785.
65 D. Xu, M. Ding, X. Hong, G. Liu and S. C. E. Tsang, *ACS Catal.*, 2020, **10**, 5250–5260.
66 X. Wang, P. J. Ramírez, W. Liao, J. A. Rodriguez and P. Liu, *J. Am. Chem. Soc.*, 2021, **143**, 13103–13112.
67 C.-S. Chen, W.-H. Cheng and S.-S. Lin, *Appl. Catal., A*, 2003, **238**, 55–67.
68 G. R. Sheffer and T. S. King, *J. Catal.*, 1989, **115**, 376–387.
69 G. R. Sheffer and T. S. King, *J. Catal.*, 1989, **116**, 488–497.

70 I. Chorkendorff and H. Niemantsverdriet, *Concepts of Modern Catalysis and Kinetics*, Wiley-VCH, Weinheim, Germany, 2003.
71 W. D. Mross, *Catal. Rev.*, 1983, **25**, 591–637.
72 M. P. Kiskinova, *Stud. Surf. Sci. Catal.*, 1991, **70**, 1–345.
73 W. An, F. Xu, D. Stacchiola and P. Liu, *ChemCatChem*, 2015, **7**, 3865–3872.
74 W. Liao and P. Liu, *ACS Catal.*, 2020, **10**, 5723–5733.
75 R. Shi, W. Liao, P. J. Ramírez, I. Orozco, M. Mahapatra, J. Kang, A. Hunt, I. Waluyo, S. D. Senanayake, P. Liu and J. A. Rodriguez, *Angew. Chem., Int. Ed.*, 2022, **61**, e202208666.
76 V. Mehar, W. Liao, M. Mahapatra, R. Shi, H. Lim, I. Barba-Nieto, A. Hunt, I. Waluyo, P. Liu and J. A. Rodriguez, *ACS Nano*, 2023, **17**, 22990–22998.
77 J. A. Rodriguez and F. Illas, *Phys. Chem. Chem. Phys.*, 2012, **14**, 427–438.
78 R. Shi, P. J. Ramírez, R. Rosales, M. Mahapatra, N. Rui and J. A. Rodriguez, *J. Phys. Chem. C*, 2024, **128**, 3260–3268.
79 P. Liu and J. A. Rodriguez, *J. Chem. Phys.*, 2007, **126**, 164705.
80 J. A. Rodriguez, S. Ma, P. Liu, J. Hrbek, J. Evans and M. Pérez, *Science*, 2007, **318**, 1757–1760.
81 S. P. Mehandru and A. B. Anderson, *Surf. Sci.*, 1989, **219**, 68–76.
82 J. R. B. Gomes and J. A. N. F. Gomes, *Surf. Sci.*, 1999, **432**, 279–290.
83 R. R. Contreras and A. J. Aizman, *Int. J. Quantum Chem.*, 1990, **38**, 89–96.
84 A. Kakekhani, L. T. Roling, A. Kulkarni, A. A. Latimer, H. Abroshan, J. Schumann, H. AlJama, S. Siahrostami, S. Ismail-Beigi, F. Abild-Pedersen and J. K. Nørskov, *Inorg. Chem.*, 2018, **57**, 7222–7238.
85 H. P. Bonzel, *J. Vac. Sci. Technol., A*, 1984, **2**, 866–872.
86 O. B. Christensen and J. K. Nørskov, *Chem. Phys. Lett.*, 1993, **214**, 443–446.
87 E. Broclawik, J. Datka, B. Gil, W. Piskorz and P. Kozyra, *Top. Catal.*, 2000, **11**, 335–341.
88 J. Datka, P. Kozyra and E. Kukulska-Zając, *Catal. Today*, 2004, **90**, 109–114.
89 E. Kukulska-Zając and J. Datka, *J. Phys. Chem. C*, 2007, **111**, 3471–3475.
90 E. Broclawik, J. Załucka, P. Kozyra, M. Mitoraj and J. Datka, *Catal. Today*, 2011, **169**, 45–51.
91 H. Yang, Y. Chen, X. Cui, G. Wang, Y. Cen, T. Deng, W. Yan, J. Gao, S. Zhu, U. Olsbye, J. Wang and W. Fan, *Angew. Chem., Int. Ed.*, 2018, **57**, 1836–1840.
92 W. An, A. E. Baber, F. Xu, M. Soldemo, J. Weissenrieder, D. Stacchiola and P. Liu, *ChemCatChem*, 2014, **6**, 2364–2372.
93 B. Yoon, H. Häkkinen, U. Landman, A. S. Wörz, J.-M. Antonietti, S. Abbet, K. Judai and U. Heiz, *Science*, 2005, **307**, 403.
94 Y.-P. Ma and G.-C. Wang, *J. Mol. Model.*, 2023, **29**, 375.
95 S. Kattel, P. Liu and J. G. Chen, *J. Am. Chem. Soc.*, 2017, **139**, 9739–9754.
96 R. C. E. Hamlyn, M. Mahapatra, I. Orozco, I. Waluyo, A. Hunt, J. A. Rodriguez, M. G. White and S. D. Senanayake, *J. Phys. Chem. C*, 2020, **124**, 3107–3121.
97 W. Li, G. Zhang, X. Jiang, Y. Liu, J. Zhu, F. Ding, Z. Liu, X. Guo and C. Song, *ACS Catal.*, 2019, **9**, 2739–2751.
98 Y. Zang, Z. Zhang, J. Qu, F. Gao, J. Gu, T. Wei and X. Lin, *J. Colloid Interface Sci.*, 2024, **658**, 167–178.
99 S. Li, Y. Xu, H. Wang, B. Teng, Q. Liu, Q. Li, L. Xu, X. Liu and J. Lu, *Angew. Chem., Int. Ed.*, 2023, **62**, e202218167.
100 P. R. Khangale, *Catal. Lett.*, 2022, **152**, 2745–2755.
101 Z. Zhang, X. Hu, Y. Wang, S. Hu, J. Xiang, C. Li, G. Chen, Q. Liu, T. Wei and D. Dong, *Fuel*, 2019, **237**, 566–579.
102 P. R. Khangale, R. Meijboom and K. Jalama, *Catal. Lett.*, 2021, **151**, 3396–3403.
103 H. Jo, H.-J. Chun, J. R. Sugiarto, M. K. Khan, M. Irshad, W. Yoon, S. K. Kim and J. Kim, *Appl. Catal., B*, 2024, **359**, 124457.
104 X. Chen, R. Gao, Q. Wang, K. Hu, F. Wang, C. Deng, L. Xu, C. Zhang, K.-W. Jun, S. Ki Kim, T. Zhao, H. Wan and G. Guan, *Fuel*, 2024, **364**, 131061.
105 J. Zhu, P. Wang, X. Zhang, G. Zhang, R. Li, W. Li, T. P. Senftle, W. Liu, J. Wang, Y. Wang, A. Zhang, Q. Fu, C. Song and X. Guo, *Sci. Adv.*, 2022, **8**, eabm3629.
106 Y.-X. Wang and G.-C. Wang, *J. Phys. Chem. C*, 2022, **126**, 17579–17588.
107 C. Ye, F. Dattila, X. Chen, N. López and M. T. M. Koper, *J. Am. Chem. Soc.*, 2023, **145**, 19601–19610.
108 X. W. Nie, L. L. Meng, H. Z. Wang, Y. G. Chen, X. W. Guo and C. S. Song, *Phys. Chem. Chem. Phys.*, 2018, **20**, 14694–14707.
109 M. S. Duyar, C. Tsai, J. L. Snider, J. A. Singh, A. Gallo, J. S. Yoo, A. J. Medford, F. Abild-Pedersen, F. Studt, J. Kibsgaard, S. F. Bent, J. K. Nørskov and T. F. Jaramillo, *Angew. Chem., Int. Ed.*, 2018, **57**, 15045–15050.
110 A. Andersen, S. M. Kathmann, M. A. Lilga, K. O. Albrecht, R. T. Hallen and D. Mei, *Catal. Commun.*, 2014, **52**, 92–97.
111 S. C. Ammal and A. Heyden, *ACS Catal.*, 2019, **9**, 7721–7740.
112 H. Zhang and P. Liu, *Chem. Catal.*, 2025, **5**, 101156.
113 B. Eren, D. Zherebetskyy, L. L. Patera, C. H. Wu, H. Bluhm, C. Africh, L.-W. Wang, G. A. Somorjai and M. Salmeron, *Science*, 2016, **351**, 475–478.
114 L. Xu, K. G. Papanikolaou, B. A. J. Lechner, L. Je, G. A. Somorjai, M. Salmeron and M. Mavrikakis, *Science*, 2023, **380**, 70–76.
115 D. Cheng, Z. Wei, Z. Zhang, P. Broekmann, A. N. Alexandrova and P. Sautet, *Angew. Chem., Int. Ed.*, 2023, **62**, e202218575.
116 S. Jensen, R. Cheula, M. Hedevang, M. Andersen and J. V. Lauritsen, *Angew. Chem., Int. Ed.*, 2024, **63**, e202405554.
117 Z. Zhang, W. Gee, P. Sautet and A. N. Alexandrova, *J. Am. Chem. Soc.*, 2024, **146**, 16119–16127.
118 D. B. Clarke and A. T. Bell, *J. Catal.*, 1995, **154**, 314–328.
119 G. J. Millar, C. H. Rochester and K. C. Waugh, *J. Catal.*, 1995, **155**, 52–58.
120 L. Barberis, C. I. Versteeg, J. D. Meeldijk, J. A. Stewart, B. D. Vandegehuchte and P. E. de Jongh, *ACS Catal.*, 2024, **14**, 9188–9197.
121 C. Burda, X. Chen, R. Narayanan and M. A. El-Sayed, *Chem. Rev.*, 2005, **105**, 1025–1102.

122 X. Rong, H.-J. Wang, X.-L. Lu, R. Si and T.-B. Lu, *Angew. Chem., Int. Ed.*, 2020, **59**, 1961–1965.
123 L. Liu and A. Corma, *Chem. Rev.*, 2018, **118**, 4981–5079.
124 C. Xia, Y. Qiu, Y. Xia, P. Zhu, G. King, X. Zhang, Z. Wu, J. Y. Kim, D. A. Cullen, D. Zheng, P. Li, M. Shakouri, E. Heredia, P. Cui, H. N. Alshareef, Y. Hu and H. Wang, *Nat. Chem.*, 2021, **13**, 887–894.
125 B. An, Z. Li, Y. Song, J. Zhang, L. Zeng, C. Wang and W. Lin, *Nat. Catal.*, 2019, **2**, 709–717.
126 H. Wang, X. Nie, Y. Chen, X. Guo and C. Song, *J. CO_2* Util., 2018, **26**, 160–170.
127 A. Bansode, B. Tidona, P. R. von Rohr and A. Urakawa, *Catal. Sci. Technol.*, 2013, **3**, 767–778.
128 S. Das, M. Sengupta and A. Bordoloi, *ChemCatChem*, 2017, **9**, 1845–1853.
129 S. J. Ahlers, M. M. Pohl, M. Holena, D. Linke and E. V. Kondratenko, *Catal. Sci. Technol.*, 2016, **6**, 2171–2180.
130 J. Wang, T. Wang, Y. Xi, G. Gao, P. Sun and F. Li, *Angew. Chem., Int. Ed.*, 2023, **62**, e202311335.
131 P. Tian, M. Gu, R. Qiu, Z. Yang, F. Xuan and M. Zhu, *Ind. Eng. Chem. Res.*, 2021, **60**, 8705–8713.
132 R. Liu, D. Leshchev, E. Stavitski, M. Juneau, J. N. Agwara and M. D. Porosoff, *Appl. Catal., B*, 2021, **284**, 119787.
133 M. E. Gálvez, S. Ascaso, P. Stelmachowski, P. Legutko, A. Kotarba, R. Moliner and M. J. Lázaro, *Appl. Catal., B*, 2014, **152–153**, 88–98.

